PALLADIUM NANOSHEETS CATALYZED FORMIC ACID OXIDATION AND CO_2 REDUCTION

By

Wenqi Zhou

A thesis submitted to Johns Hopkins University in conformity with the requirements for the degree of Master of Science in Engineering

Baltimore, Maryland

May 2020

Abstract

Human society has been relied on the combustion of fossil fuel as the primary energy source for a long time, yet this has led to great emission of CO_2 and corresponding environmental problems like global warming. Among all the technologies that have been developed to decrease the dependence on fossil fuel and alleviate the greenhouse effects, combing the electrochemical CO_2 reduction and fuel cell applications could be a promising solution.

Electrochemical CO_2 reduction is an artificial way of carbon cycling. If supported by the renewably sourced electricity, the intermittent renewable energy could be stored in the form of chemical bond in the CO_2 reduction products, part of which could be applied to fuel cells for efficient energy conversion and long-term energy consumption. In this way, a fossil fuel-free and economic energy cycle can be realized. Formic acid could be a target fuel to achieve this approach, since it is a common product in CO_2 reduction and possesses high energy density as well as less membrane crossover problem when applied to fuel cells. One major challenge for the scale application of this idea is the large overpotential and low selectivity towards the electrochemical reaction, therefore it is desirable to develop bi-functional catalysts with high selectivity and activity towards formic acid in CO_2 reduction, while also have excellent performance in the formic acid fuel cells.

The work performed within this thesis reports a novel method to synthesize Pd nanosheets (Pd NSs) with different thickness and intrinsic in-plane compressive strain, as well as Au@Pd nanosheets. Their performance as electrocatalysts for formic acid oxidation (FAOR) and CO_2 reduction reaction (CO_2RR) have been evaluated. The activity of Pd NSs towards FAOR were demonstrated to be higher than that of commercial Pd, and growing gold on the Pd NSs could lead

to a product selectivity change, suggesting that Pd-based nanosheets could be regarded as promising catalysts for electrochemical CO_2 reduction and fuel cell application.

Advisor: Dr. Chao Wang

Reader: Dr. Anthony Shoji Hall

Acknowledgements

I would like to acknowledge my academic advisor Prof. Chao Wang for his continuous support and guidance for my study and research during the past two year. It is under his supervision that I have built up an insightful understanding of electrocatalysis. The skills, knowledge, professionalism and experience that I've harvested in the Wang lab are things I'll cherish for the rest of my life.

I would like to express my deepest appreciation to Fei Xu, whom I worked with for this project. He is a great mentor as well as a reliable friend. His guidance helped me in all the time of research and writing of this thesis. The next person I would like to give a specific appreciation is Dr. Yifan Liu, whom I worked with during the first master year, it would be impossible to count all the ways that he has helped me in my life. Other members in Wang Lab have also provided me with abundant help. I would like to thank Hao Shen for his advice on my thesis defense, Akshat Vij for every encouragement he gave before my group presentation, and Liyin Zhang for all the time we were working together.

I would like to thank my best friend and roommate Liyi Xu for what we've been through in the past two years, as well as all the thoughts, desires, expectations and joy we have shared with each other. Lastly and most importantly, I would like to express my gratitude to my parents Mr. Zhou and Mrs. Wen. Thank you for your love and tolerance that supported me all the way along this journey.

Contents

List of tables

List of figures

1. Introduction

1.1 Motivation

The purpose behind the work presented in this thesis is to develop bi-functional catalysts towards formic acid oxidation and CO_2 reduction for fulfilling the goal of fossil fuel-free and efficient energy recycle. Nanomaterial synthesis and electrochemical catalytic performance were studied to seek the link between the material structure, component and catalytic activity.

This thesis presents the synthesis of Pd nanosheets (Pd NSs) as electrocatalysts for formic acid oxidation and gold growing on the Pd NSs (Au@Pd NSs 2) for the CO_2 reduction. Meticulously designed free-standing two-dimensional nanosheets with tunable intrinsic strain were synthesized through organic solvothermal method, and characterized by Transmission Electron Microscopy (TEM), High Resolution Transmission Electron Microscopy (HRTEM), Inductively Coupled Plasma Mass Spectrometry (ICP-MS), Energy Dispersive X-ray Spectrometry (EDS). Comprehensive evaluation of their catalytic performance in terms of activity, stability, selectivity has been conducted.

The remainder of this introduction is presenting the fundamental of nanomaterial synthesis, two-dimensional nanomaterials and intrinsic stain effect, direct formic acid fuel cells and formic acid oxidation reaction, greenhouse effect and CO_2 electrochemical reduction.

1.2 Principle of nanomaterial synthesis

Nanomaterials are one of the novel materials that has seized the attention of scientific community for a long time due to the unique physical, chemical and biological properties endowed by their nano-range scale (1-100 nm). Tuning their size and shape to alter those properties offers numerous surprising discoveries and displays great potential for applications, such as nanostructures for diagnostic and therapy, engineered nanomaterials for papermaking, functional thin film for sensors, nanomaterials for catalysis and energy conversion[1]. The synthesis of nanomaterials generally includes two categories: "Top down" and "Bottom up". "Top Down" approach mainly utilizes physical ways breaking the bulk material into nanoscale one, including low temperature crushing, ultrasonic pulverization, ball milling, photolithograph etc. One problem of this method is the inhomogeneity of sizes and shapes, restricted by the physical condition and technique. In contrast, "Bottom up" method provides the possibility of creating more size and shape-controlled nanostructures, by taking the advantage of atoms and molecules self-assembly or other physiochemical reactions. Typical "Bottom up" method involves solvothermal method, chemical vapor deposition (CVD)[2], physical vapor deposition (PVD)[3] etc. Among these method, solvothermal method is the one that has usually been used in the laboratory to synthesize nanomaterials, due to the ease and preciseness of controlling size, morphology distribution and crystallinity, by changing the reaction temperature, reaction time, precursor and surfactant. Figure 1.1 shows a common experimental setup of organic solvothermal synthesis, with thermometer, magnetic stirring and certain atmosphere.

Figure 1.1 Photo of organic solvothermal synthesis experimental setup.

The solvothermal synthesis of nanomaterials involves the reactions where the dispersed atoms, ions or molecules gradually gather and grow, generally including two processes: nucleation and Ostwald ripening. When sufficient metal salt precursors are added into solvent and under appropriate temperature, the whole system is in a nonequilibrium condition. Atoms or molecules begin to aggregate to relieve the supersaturation and try to move the whole system towards equilibrium, leading to the formation of nuclei, the birth of which in a metastable phase is called nucleation[4]. It's a fast process that all the metal salt precursors would be consumed in a rather short period, accompanying with slightly increased nuclei radius and the formation of small nanoparticle[5] (see in Figure 2.1). Then these nuclei and nanoparticles will go through the spontaneous Ostwald ripening process: sacrificing small particles to generate larger particles, because large particles are more energetically favored from a thermodynamic perspective. Therefore, the nanoparticles will gradually have more uniform size and shape.

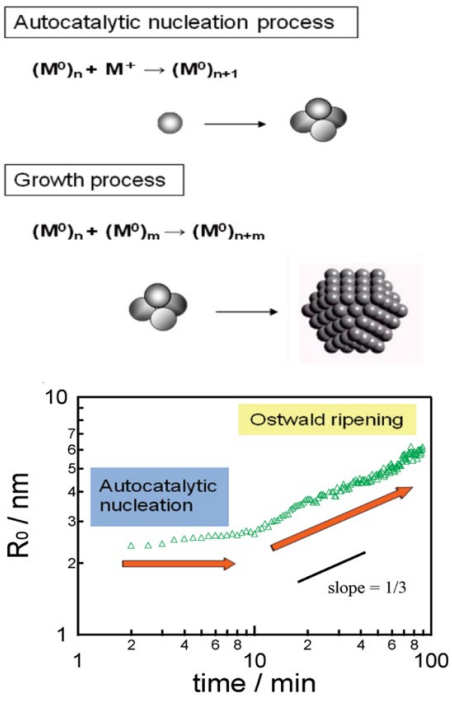

Figure 1.2 Schematic illustration for nucleation process of Ag nanoparticle. Adapted with permission from ref[5]. Copyright 2010 American Chemical Society.

1.3 Two-dimensional nanomaterials and strain effects

Two-dimensional (2D) nanomaterial is a newly developed material that possesses sheet-like structure, with lateral size usually larger than 100 nm, and ultrathin thickness of one or a few atomic atom[6]. One typical sign of this structure is the extension of strong covalent binding through the plane and weak van der Waals interaction between atomic layers[7]. Since the discovery of exfoliated graphene in 2004, great attentions have been paid to the research concerning the ultrathin 2D materials, including metal-free 2D materials, metal chalcogenides, transition-metal oxides and hydroxides, MXenes and non-layered transition metal carbides and nitrides, transition metals, metal-organic frameworks (MOFs) and covalent-organic frameworks (COFs)[8]. Some examples of these 2D structural configurations are showed in Fig 1.3[7]. Since electrons are

restrained in the two-dimensional environment, this type of materials exhibit unique physical and chemical properties compared with bulk materials, and great potential for wide application like optoelectronic devices, catalysis, energy storage and conversion, sensors and biomedicine.

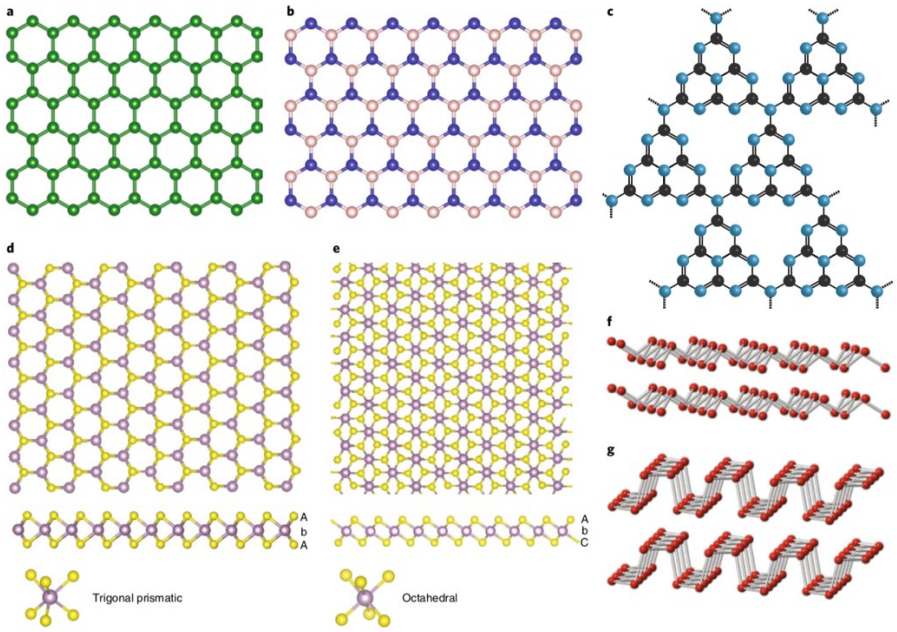

Figure 1.3 Schematic structural configurations of 2d materials. (a) graphene. (b) h-bn. (c) heptazine-based g-c_3h_4. (d) TMDs as exemplified by mos_2 in 2H-phase (e) and 1T-phase. (f) black phosphorus and pnictogens in rhombohedral and (g) orthorhombic phases. Adapted with permission from ref [7]. Copyright 2018 Nature Catalysis.

For catalysis, the 2D materials have the advantages over others in three main aspects: specific surface area, mechanical properties, electron and thermal conductivity[7]: because of the ultrathin structure, 2D materials usually have large surface to bulk ratio, namely more surface-active sites could be exposed during the catalysis process. Superior mechanical property endows them with durability in harsh condition, and thermal conductivity could facilitate the diffusion of heat in exothermic reaction. Additionally, the catalytic performance could be tailored by the tunable electron properties, through the utilization of heteroatom doping, defect engineering,

lateral size and thickness regulation, interface engineering, strain and phase engineering[8]. These tailored 2D materials have been widely explored as electrocatalysts for several important catalytic reaction including carbon dioxide reduction reaction (CO_2RR), hydrogen evolution reaction (HER), oxygen evolution reaction (OER) and oxygen reduction reaction (ORR), etc.

Lattice stain alteration is a typical method applied to change the electronic states of the materials, and many studies have displayed the possibility of improving catalytic performance with this strategy. For example, the research work this dissertation is following demonstrated that an atomic-level control of palladium (110) nanosheets thickness would enable the generation and fine-tuning of intrinsic strain to optimize catalytic reactivity towards ORR and HER, with more than an order magnitude activity enhancement, when comparing with the nanoparticle counterpart[9]. One highlight of this study is utilizing the surface stress to drive intrinsic strain in free-standing nanosheets, instead of overlaying the catalyst on a substrate, which would easily lead to problems like mechanical instability, dissolution around the interface, surface ligand effect and production of surface alloy. The basic mechanism for the intrinsic strain generation is as following: the cleavage of bulk materials to from a new surface usually results in charge redistribution and attractive interactions between surface atoms, manifested as tensile surface stress, which could induce a pressure at the order of 10^5 atm on the surface atom. Though it has little effect on the structure with macroscopic thickness, it could remarkably affect the ultrathin 2D structures and lead to in-plane compressive strain, strongly depending on the slab thickness, as shown in Fig 1.4[9].

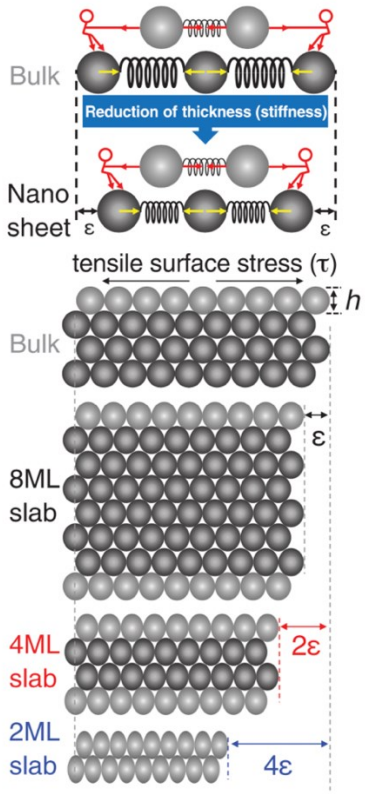

Figure 1.4 Mechanism of the generation of intrinsic strain in two-dimensional transition metal nanosheets. h is the height of an atomic layer, ε represent the lattice strain, τ is the tensile surface stress. Adapted with permission from ref [9]. Copyright 2019 Science.

1.4 Direct formic acid fuel cells and formic acid oxidation reaction

Fuel cells are devices that directly undergo a chemical process converting the chemical energy in hydrogen or other fuels into electricity. Unlike batteries, fuel cells need no periodical recharging process, and will provide electricity ceaselessly as long as the fuel is consistently be replenished. Compared with the traditional combustion-based devices, the advantages of fuel cells are mainly reflected in three aspects[10]: the first one is high energy conversion efficiency, which can reach up to 60 %. The second superiority of fuel cells is lower emission property, particularly

displayed in the hydrogen fuel cells, the only final product of which is water and there are no air pollutants generated triggering health problem. Besides, fuel cells are near-silent during operation since they have less moving part. Due to these benefits, fuel cells have already been adopted to a wide range of applications, as shown in Figure 1.5, from power station, transportation vehicles to portable laptop computer.

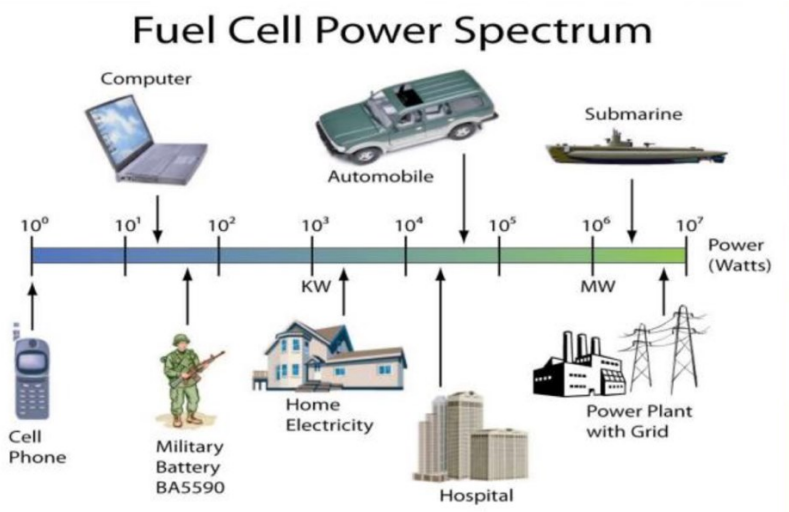

Figure 1.5 Schematic illustration of fuels cell application and corresponding power.source: https://www.slideserve.com/noelani-eaton/fuel-cell-overview.

Among all fuels, hydrogen is the cleanest with only water as anodic reaction product, and it has the highest energy per mass of any fuel. However, one problem that hinders hydrogen application in fuel cells is the difficulty in its transportation and storage: storing in gas phase requires high press tanks (5000 -10000 psi tank pressure), while in liquid phase demands cryogenic temperatures[11]. Other liquid fuels can be more convenient choice for anodic feed in fuel cell. Regarding liquid fuel cells, direct methanol fuel cells (DMFCs) have been most extensively studied. However, one issue for DMFCs is the ease permeation of methanol to cathode through the Nafion membranes, resulting in fuel loss[12]. To alleviate this adverse effects, diluted methanol is feed yet sacrificing the overall energy density of the system. Compare with methanol, formic

acid (FA) has considerably less crossover through Nafion membranes and is non-toxic[13]. It is a major by-product of petroleum refinery, biomass processing and other organic synthesis process, also common in nature[14]. Direct reduction of CO_2 can generate formic acid either. Together with high energy density (1725 Wh/kg, 2104 Wh/L)[15] and the property of easier handling than hydrogen, formic acid can be a promising chemical fuel for fuel cells.

Belonging to proton exchange membrane fuel cells (PEMFCs), direct formic acid fuel cell (DFAFC) is composed of an anode, a cathode and a polymer electrolyte membrane. Formic acid is channeled to the anode, where the direct oxidation of formic acid into carbon dioxide releases two electrons per molecule. The polymer electrolyte membrane allows the positively charged protons instead of electrons to pass through to the cathode. The negatively charged electrons flow through an external circuit, forming electrical current. At the cathode, through a four electron/proton - coupled reaction (ORR), oxygen is reduced to form water and heat. The anode, cathode, overall reaction formulas and standard reaction potentials in acid environment can be described as followings[15]:

Anode: $HCOOH \rightarrow CO_2 + 2H^+ + 2e^-$ $E^0 \sim -0.25$ V (vs SHE)

Cathode: $\frac{1}{2} O_2 + 2H^+ + 2e^- \rightarrow H_2O$ $E^0 = 1.229$ V (vs SHE)

Overall: $HCOOH + \frac{1}{2} O_2 \rightarrow CO_2 + H_2O$ OCV ~ 1.48 V

Currently three possible mechanisms of formic acid oxidation reaction have been proposed, as shown in equation (1) to (3): $*$ represents the molecule in an absorbed state[16]. Equation (1) shows a direct pathway, where the removal of the first proton comes from the cleavage of C-H bond, producing hydroxy carbonyl. Then the second dehydrogenation occurs at O-H bond, resulting in the formation of CO_2. The equation (2) is referred as formate pathway. The

dehydrogenation position before and after exchanges, with the first cleavage happened in O-H bond to produce formate, and then at C-H bond to generate CO_2. Though mechanism 1 and 2 sometimes are referred as "direct pathway" jointly, since they all go through the dehydrogenation process to produce carbon dioxide directly, though via different intermediates. Equation (3) is called indirect pathway, where CO∗ is generated through the non-faradaic dehydration reaction of formic acid, and further be oxidized to form CO_2. In this pathway, the generation of CO intermediate has strong adverse poisoning effects on catalysts, leading to the problem of low activity.

Direct pathway:

$$HCOOH* \rightarrow COOH* + H^+ + e^- \rightarrow CO_2 + 2H^+ + 2e^- \quad (1)$$

Formate pathway:

$$HCOOH* \rightarrow HCOO* + H^+ + e^- \rightarrow CO_2 + 2H^+ + 2e^- \quad (2)$$

Indirect pathway:

$$HCOOH* \rightarrow CO* + H_2O \rightarrow CO_2 + 2H^+ + 2e^- \quad (3)$$

1.5 Greenhouse effect and CO_2 electrochemical reduction

Today, non-renewable fossil fuels are the main primary energy source for human society. According to a statistics and prediction of world energy consumption by energy sources: coal, petroleum and natural gas together has an 80% share and will continue to be the main supply in recent 30 years (as shown Fig 1.6). Though fossil fuel provide most of the electricity, heat and transportation, while also facilitating the human production from steel to plastics, there are environmental consequences for utilizing them: the combustion of fossil fuel releases carbon dioxide (CO_2) and other greenhouse gas, which could not be absorbed by vegetation and the oceans,

accumulating in the earth atmosphere trapping excessive infrared heat (Fig 1.7), contributing to the global warming and climate change.

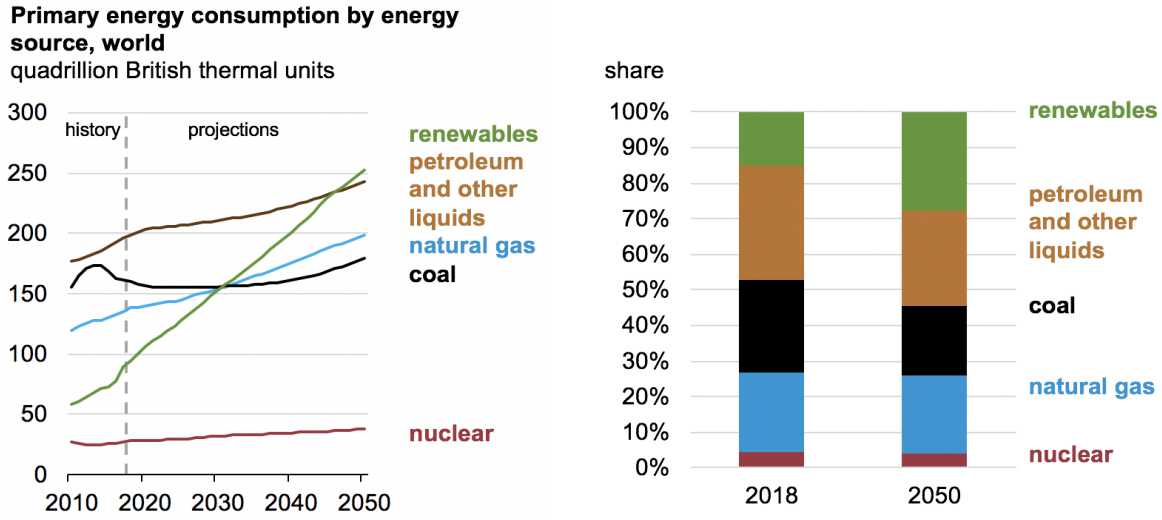

Figure 1.6 History and projection of primary energy consumption by energy source, world.source: u.s. Energy information administration, international energy outlook 2019. Https://www.eia.gov/outlooks/ieo/pdf/ieo2019.pdf.

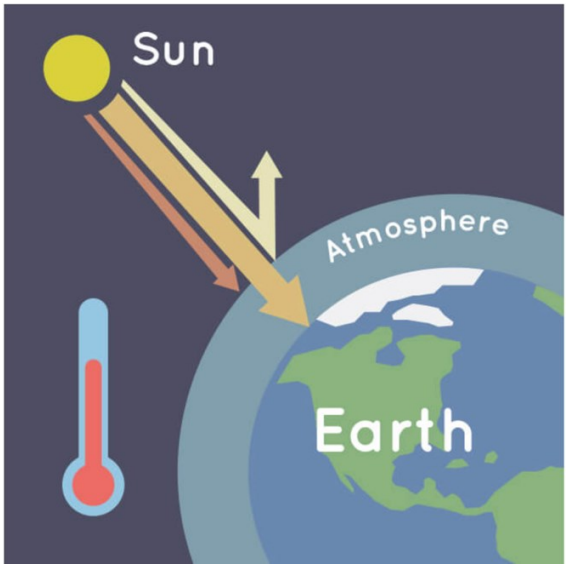

Figure 1.7 Earth atmosphere traps some of the sun's heat, preventing it from escaping back into space at night. Source: nasa, https://climatekids.nasa.gov/greenhouse-effect/.

CO_2 is the predominant component of greenhouse gas, taking over 81 % of the total emission, largely due to the fossil fuel combustion for transportation and electricity (Fig 1.8). According to the data from NASA, the atmospheric CO_2 level has been showing an increasing tendency, from around 380 parts per million (ppm) in 2005 to 413 ppm in March 2020 (Fig 1.9). The accompanying global warming has been intuitively showed in Fig 1.10. An approximate 96 mm rising of sea level has also been observed from 1993 to 2019 by satellites, because of two factors related to the global warming: the expansion of sea water as it is getting warmer and the melting glaciers. Based on the observation, the sea level is predicted to rise continually at a rate of 3.3 millimeters per year[17]. All of these would bring the society irreparable losses, leading to the development of new alternative energy technologies.

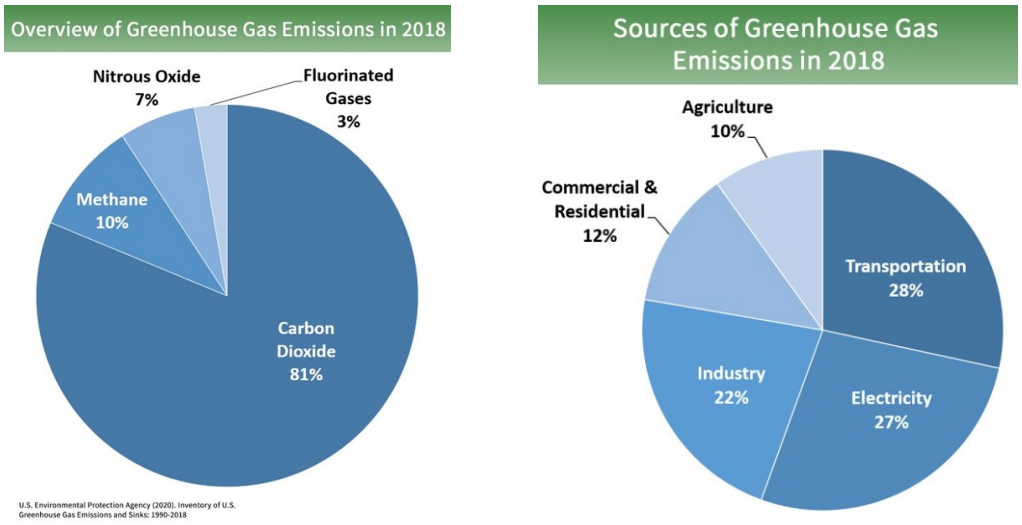

Figure 1.8 Overview of greenhouse gas emission (left) and source of greenhouse emission (right) in 2008. Source: inventory of u.s. Greenhouse gas emissions and sinks, https://www.epa.gov/ghgemissions/inventory-us-greenhouse-gas-emissions-and-sinks.

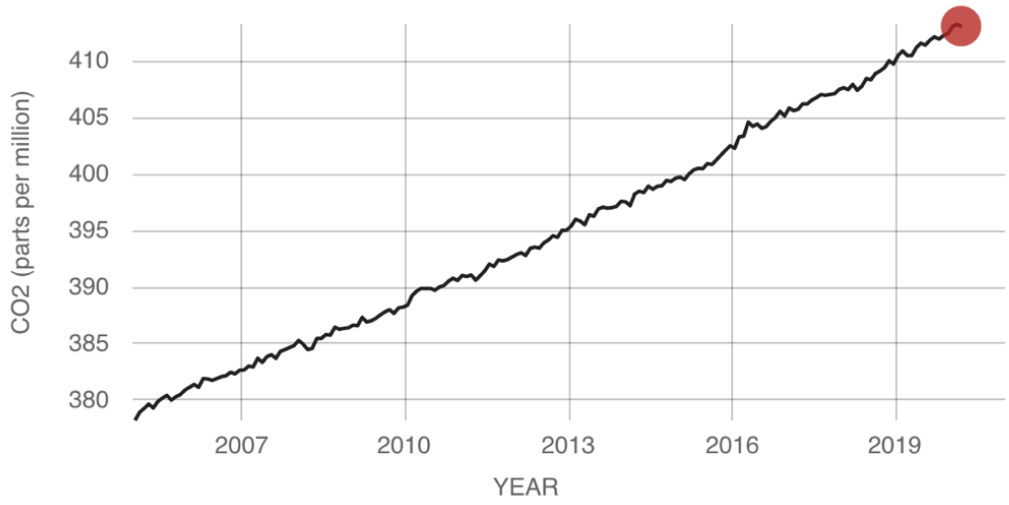

Figure 1.9 Atmospheric CO_2 levels measured at mauna loa observatory, hawaii, from 2015-present. Source: NASA, https://climate.nasa.gov/vital-signs/carbon-dioxide/.

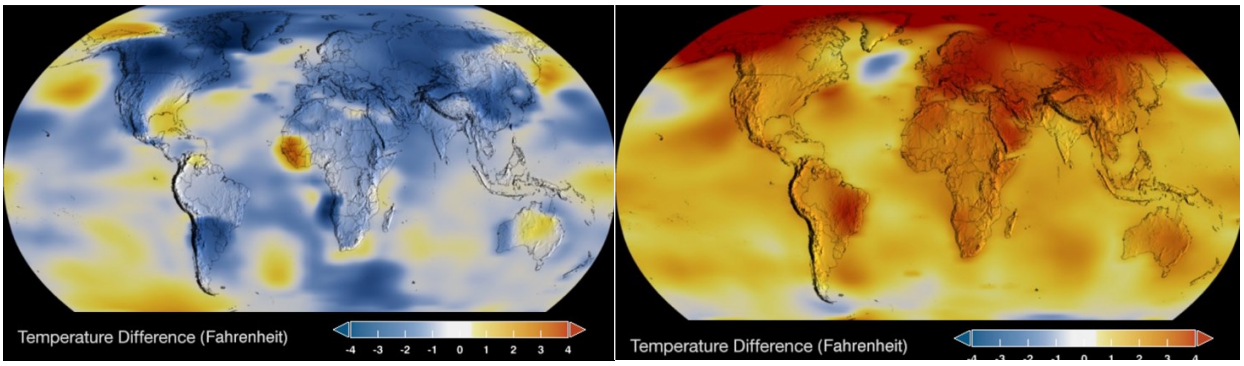

Figure 1.10 Average variation of global surface temperature in 1884 (left) and 2019 (right): dark blue indicates areas cooler than average, and dark red indicates areas warmer than average. Sour: NASA, https://climate.nasa.gov/vital-signs/global-temperature/.

To tackle the problem, the development of renewable energy such as solar, geothermal and wind energies has come into our focus and is growing up rapidly. However, due to the intermittent

nature, the renewable electricity generated is hard to merge into the electrical grid due to the intermittent nature[18]. The further large-scale application has also been impeded by the insufficiency of high-efficiency energy storage and conversion techniques. Therefore, instead of trying to replace fossil fuel with new energy sources, there are techniques seeking to change how the fuel is derived. Electrochemically reduction of CO_2 to fuels and commodity chemicals, with water as hydrogen source and powered by the intermittent electricity could be a promising approach, which creates a closed recycle of CO_2 utilization as shown in Fig 1.11[19].

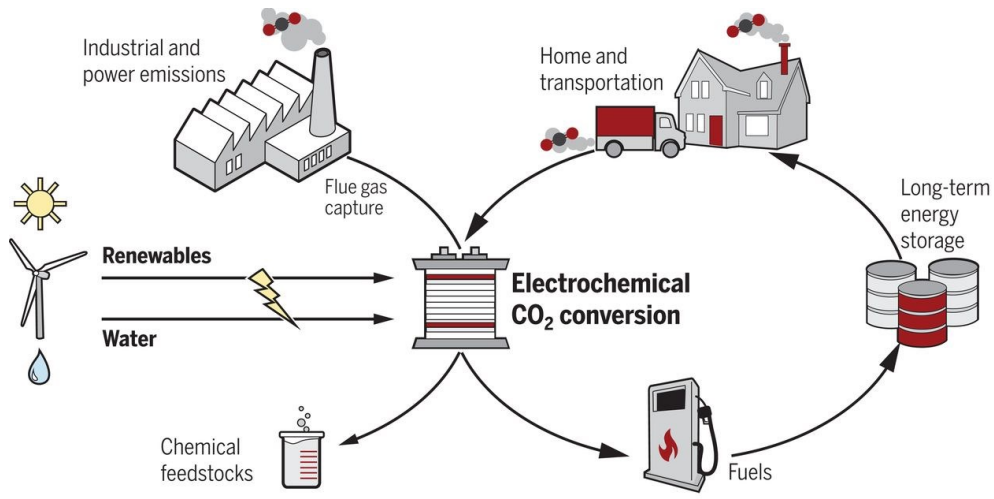

Figure 1.11 Schematic illustration showing the reduction of CO_2 using renewably sourced electricity could transform waste CO_2 emission into commodity chemical feedstocks for fuel. Adapted with permission from ref [19]. Copyright 2019 Science.

The electrochemical reduction of CO_2 has the advantages over other technologies in several aspects: First, it can be driven by renewable intermittent energy, which is stored in the form of chemical bond in the reduction products. It would be much easier to utilize the existing

infrastructures to transport and store these products. Second, the electrolyte and catalysts applied in the CO_2 reduction fuel cell (CRFC) are generally innocuous, therefore the safety regarding the waste disposal is not big concern. Besides, there is hidden economic value behind the CO_2 electrochemical reduction. It has been demonstrated that up to 18 different products could be produced through CO_2 reduction within a range of 600 mV[20]. The market prices and annual global production of the main reduction products are showed in Fig 1.12, illustrating their monetary sense and the importance of tuning the selectivity of CO_2 reduction.

product	number of required electrons	market price ($/kg)	normalized price ($/electron) × 10^3	annual global production (Mtonne)
carbon monoxide (syngas)	2	0.06	0.8	150.0
carbon monoxide	2	0.6	8.0	
formic acid	2	0.74	16.1	0.6
methanol	6	0.58	3.1	110.0
methane	8	0.18	0.4	250.0
ethylene	12	1.30	3.0	140.0
ethanol	12	1.00	3.8	77.0
n-propanol	18	1.43	4.8	0.2

Figure 1.12 Market price and annual global production of the co2 reduction products. Source: Royal Society of Chemistry, https://www.chemistryworld.com/news/can-catalysis-save-us-from-our-co2-problem/3010555.article.

Though electrochemical reduction of CO_2 is very promising alternative technology, there are several hurdles for its scale application: sluggish kinetics, large overpotential required for the high-value product, along with the lack of selectivity for desired product (low faradaic efficiency). It is well known CO_2 reduction product distribution is closely linked to the CO adsorption property

of a given metal catalyst[21]: Metals that are weakly bind to CO such as Sn and Hg, were found to be active at low overpotential, being uncapable of breaking the C-O bond, producing only formate. On strongly binding metals like Pt and Ni, surface CO poisoning is highly prone, catalytic activity will be diminished very quickly. Only metals with intermediate CO binding energy like Au, Ag and Cu are capable of further reducing CO to get more advanced products like methane, ethylene. Since the electrochemical CO_2 reduction is often conducted in aqueous electrolyte, the competing hydrogen evolution reaction (HER) will also influence the selectivity towards products. Since it has simpler mechanism and is more favored from thermodynamic perspective, when compared with some CO_2 reduction process. The formulas and equilibrium potentials for the major half-cell reactions mentioned above, as well as HER in standard condition, are showed as following:

$$CO_2 + 2H^+ + 2e^- \rightarrow CO + H_2O \quad E_0 = -0.103\ V\ vs.\ SHE$$

$$CO_2 + H^+ + e^- \rightarrow HCOO^- + H_2O \quad E_0 = -0.225\ V\ vs.\ SHE$$

$$2CO_2 + 12H^+ + 12e^- \rightarrow C_2H_4 + 2H_2O \quad E_0 = 0.079\ V\ vs.\ SHE$$

$$CO_2 + 8H^+ + 8e^- \rightarrow CH_4 + 2H_2O \quad E_0 = 0.169\ V\ vs.\ SHE$$

For palladium catalyzed CO_2 reduction, formate, CO and H_2 are the major reported product[22]. One problem for Pd catalyst is their relative strong binding to CO, which could lead to the surface poisoning and deactivation[23]. Synergistic effect has been applied to mitigate this problem and increase the faradaic efficiency for specific product. Kortlever, Ruud, et al[24] have reported PdPt/C nanoparticles with low onset potential for the reduction of CO_2 to formic acid in a pH 6.7 phosphate buffer (0.1 M KH_2PO_4/0.1 M K_2HPO_4). The formic acid production is starting from 0 V vs. RHE, very close to the theoretical value. By tuning the Pd content, the $Pd_{70}Pt_{30}$/C nanoparticles exhibited good faradaic efficiency (FE) towards formic acid and capability of

avoiding fast poisoning. As shown in Fig 1.13, a maximum FE of 90% was recorded at the applied potential of -0.4 V vs. RHE during one-hour electrolysis. Compared with pure Pd based catalysts, the improved performance of this material has been hypothetically assigned to tuning the d-band center by mixing Pd and Pt, as well as the strain effect introduced by the addition of larger Pt atoms. Another point worth mentioning is that this PdPt/C nanoparticle could be a desirable reversible catalyst, since it also showed good performance towards formic acid oxidation reaction. Wang, Yuxuan, et al[25] reported ensemble effect in bimetallic Pd-Au electrocatalyst for CO_2 RR, the designing concept of which is tuning the dispersion and coverage of strongly CO-binding metal Pd on the weak-binding Au surface, to lower the CO_2 activation energy barrier and alleviate the CO poisoning effect, as displayed in Fig 1.14. Tested in H-type electrolysis cell with 0.1 M $KHCO_3$ as electrolyte, the CO_2 RR results showed highly dispersive Pd sites on Au nanoparticles could improve the electrocatalytic activity as well as selectivity. As shown in Fig 1.15 left, $Pd_5@Au_{95}$ was the most active one for CO_2 RR among all catalysts with same mass loading of metals and nanoparticle size, with a total CO_2 reduction current density (J_{CO2}) of 5.8 mA/cm^2_{geo} at -0.8 V vs.RHE, almost 3 times and 21 time that of pure gold and palladium respectively. In terms of FE towards CO, $Pd_5@Au_{95}$ also exhibited the best performance, reaching nearly 80% FE_{CO} at -0.5 V vs.RHE (Fig 1.15 right). DFT calculation also illustrated that the monoatomic dispersed Pd or Pd dimers could make the neighboring Au atoms have intermediate adsorption energy for ∗COOH and ∗CO, therefore accessing the best catalytic activity. Based on the research mentioned above, this dissertation has also studied the effects on CO_2RR activity and selectivity by doping gold on palladium nanosheets.

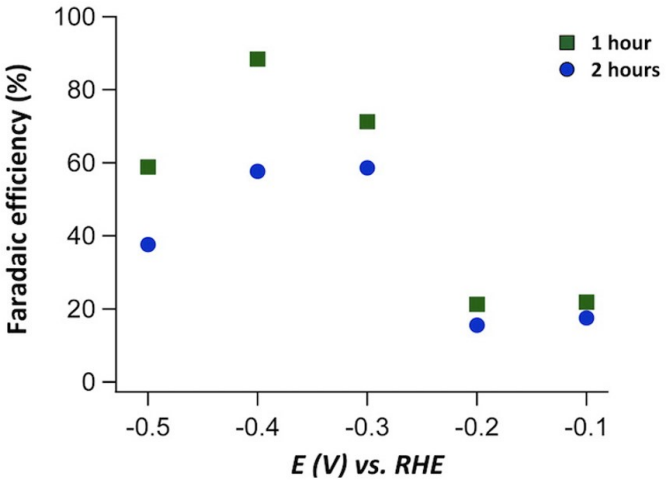

Figure 1.13 Faradaic efficiencies toward the production of formic acid on $Pd_{70}Pt_{30}$/C nanoparticles in a pH 6.7 phosphate buffer (0.1 m KH_2PO_4/0.1 m K_2HPO_4) at different potentials after 1 h (■) and after 2 h (●). Adapted with permission from ref [24]. Copyright 2015 American Chemical Society.

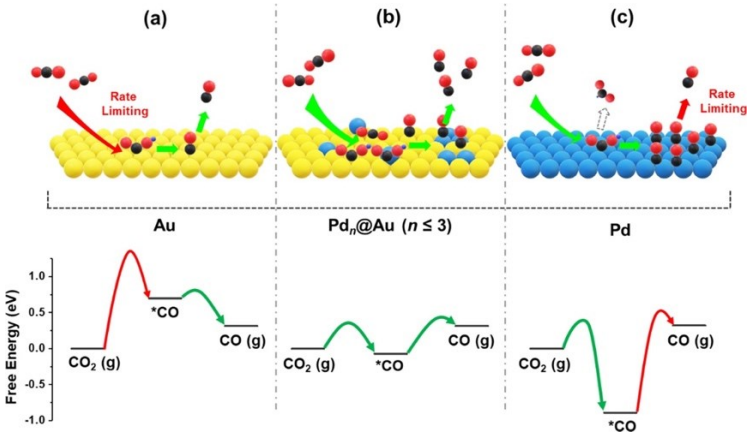

Figure 1.14 Illustration of the concept using atomically dispersed pd sites on au surface to enhance co_2 reduction: the yellow and blue spheres represent au and pd atoms, respectively. For the molecular structures, red, gray, and purple colors represent oxygen, carbon, and hydrogen, respectively. The red (vs green) arrows represent the rate-limiting factors in the reaction kinetics. Adapted with permission from ref [25]. Copyright 2019 American Chemical Society.

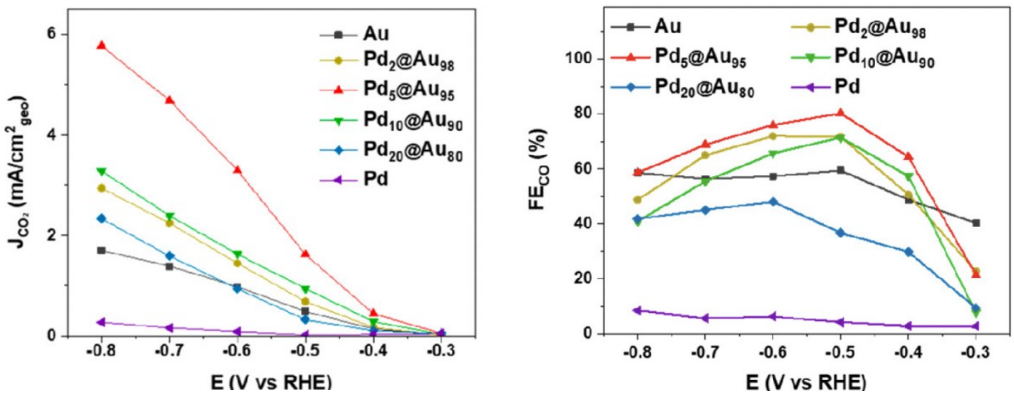

Figure 1.15 CO_2 reduction current density (jco_2) with all the carbonaceous products taken into account (left), comparison of FE toward CO (FE_{co}) for the different electrocatalysts (right). Adapted with permission from ref[25]. Copyright 2019 American Chemical Society.

2. Material and methods

2.1 Material synthesis

Materials. Oleylamine (70%, Sigma Aldrich), oleic acid (90%, Sigma Aldrich), dicobalt octacarbonyl ($Co_2(CO)_8$, with 1-5% hexane, ≥ 90%, Alfa Aesar), palladium(II) acetylacetonate ($Pd(acac)_2$, 99%, Sigma Aldrich), hydrogen tetrachloroaurate(III) hydrate ($HAuCl_4 \cdot XH_2O$, 99.8% -Au, Strem Chemicals Inc.), palladium on carbon catalyst (Pd/C, 10 wt% Pd, Alfa Aesar), nafion (5% in lower aliphatic alcohols and water (15-20%), Sigma Aldrich), hydrochloric acid (37%, Fisher Scientific), perchloric acid (70%, 99.999% trace metals basis, Sigma Aldrich), formic acid (≥ 96%, Sigma Aldrich), potassium bicarbonate (≥ 99.95% trace metals basis, Sigma Aldrich), carbon powder (Tanaka Inc.) were purchased and used as received. High purity (99.999%) argon (Ar), hydrogen (H_2), and carbon monoxide (CO) were purchased from Airgas.

In the experiment, palladium nanosheets were synthesized using CO as reducing agent and stabilizing ligand, oleylamine as solvent and surfactant, palladium (II) acetylacetonate as metal salt precursor. By changing the CO sources and temperature (Table 2.1), Pd nanosheets were fabricated with different average thickness of 3 ML, 5 ML and 8 ML (monolayer abbreviated as ML), denoted as Pd NSs 1, Pd NSs 2 and Pd NSs 3 respectively. To study the synergistic effects, gold growing on palladium nanosheets with average thickness of 5 ML (Au@Pd NSs 2) has also been synthesized successfully.

Table 2.1 Synthesis detail of Pd NSs.

	Precursors	Solvent	Temperature	Time	Reducing agent
Pd NSs 1	$Pd(acac)_2$	Oleylamine	55 ~ 60℃	3 h	CO gas
Pd NSs 2	$Pd(acac)_2$	Oleylamine	50 ~ 55℃	3 h	CO gas
Pd NSs 3	$Pd(acac)_2$	Oleylamine	50 ℃	15 min	$Co_2(CO)_8$

2.1.1 Pd NSs 1 synthesis

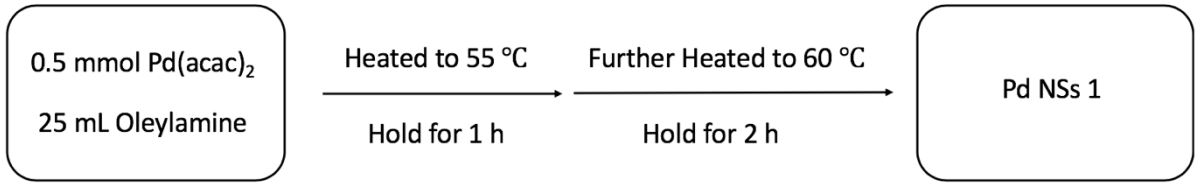

Figure 2.1 Schematic illustration of synthetic route for palladium nanosheets with average thickness of three monolayers (Pd NSs 1).

To synthesized palladium nanosheets with average thickness of 3 monolayers (Pd NSs1), palladium acetylacetonate (152 mg, 0.5 mmol) and 25 mL oleylamine were added into a four-neck flask with a typical Schlenk link setup. The mixture was under constant stirring and heated to 55 ℃ while purging with CO gas through a long hypodermic needle. After holding at 55 ℃ for 1 hour, the solution was further heated to 60 ℃ and maintained for 2 hours. The gas outlet was adjusted

to make sure the CO gas flow at a relative stable condition, with once or twice bubbling per second. As the reduction reaction proceeded, the color of the mixture would gradually change from light yellow to black. After cooling to the natural temperature, the as-prepared Pd nanosheets were collected by centrifugation and wash with 5 mL hexane and 25 mL ethanol three times, and then re-dispersed in 10 mL hexane.

2.1.2 Pd NSs 2 synthesis

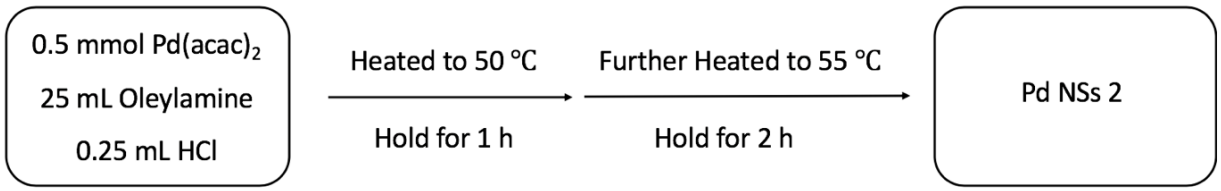

Figure 2.2 Schematic illustration of synthetic route for palladium nanosheets with average thickness of five monolayers (Pd NSs 2).

The synthesis method of palladium nanosheets with average thickness of 5 monolayers (Pd NSs 2) is similar with that of Pd NSs 1, but the differences are the addition of hydrochloric acid and temperature control. The purpose of adding hydrochloric acid is to increase the solubility of CO in the mixture, thus the palladium metal salt precursors has more exposure to the reducing agent, inducing thicker layers. Under such circumstance in order to prevent the formation of nanoparticles, the reaction was carried at lower temperature: holding at 50 ℃ for 1 hour and

maintained at 55 ℃ for another 2 hours. The as-synthesized Pd NSs 2 was also collected by washing with hexane and ethanol three times, and then re-dispersed in 10 mL hexane.

2.1.3 Pd NSs 3 synthesis

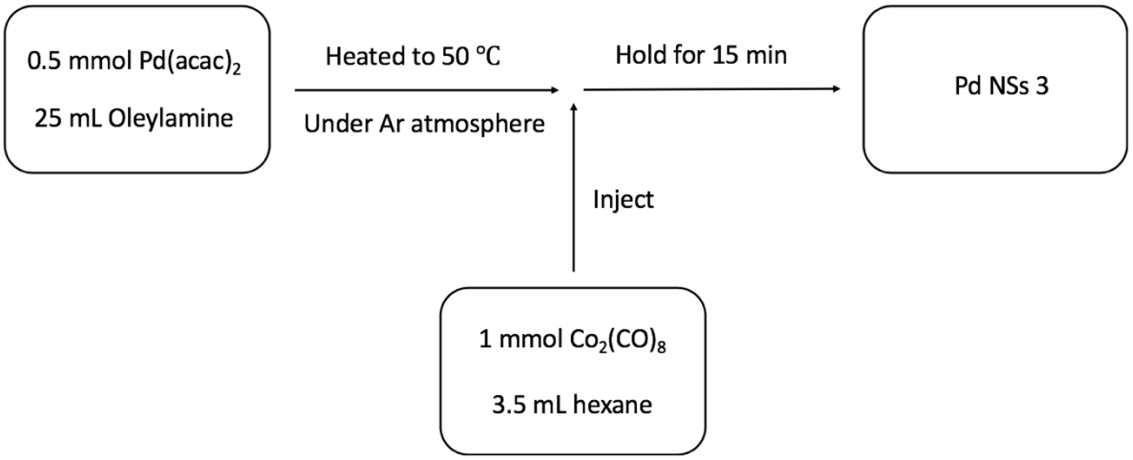

Figure 2.3 Schematic illustration of synthetic route for palladium nanosheets with average thickness of eight monolayers (Pd NSs 3).

For the synthesis of palladium nanosheets with average thickness of 8 monolayers, palladium acetylacetonate and oleylamine were still used as metal salt precursor and solvent respectively. However, instead of directly purging pure CO as reducing agent, cobalt carbonyl was used as CO source. As the mixture temperature reached 50 ℃, 345 mg cobalt carbonyl dissolved in 3.5 mL hexane was injected into the four-neck flask, at the meantime the valve of gas outlet has been closed. Since the decomposition temperature of $Co_2(CO)_8$ is around 50 ℃, the color of the mixture would turn to dark blue immediately. Because of the sudden increasing in CO concentration from the cobalt carbonyl decomposition, thicker Pd NSs were synthesized in a very

short period. Due to the same reason, the reaction temperature has also been maintained at relative low temperature 50 ℃ to avoid the generation of nanoparticles. Following the rule of classic crystal growth theory-fast growth leads to small particle size, the Pd NSs 3 has the smallest size, with an edge length around 20 nm. The natural cool-downed mixture also went through the same centrifugal washing steps, and the precipitated nanosheets were re-dispersed in 10 mL hexane.

2.1.4 Au@Pd NSs 2 synthesis

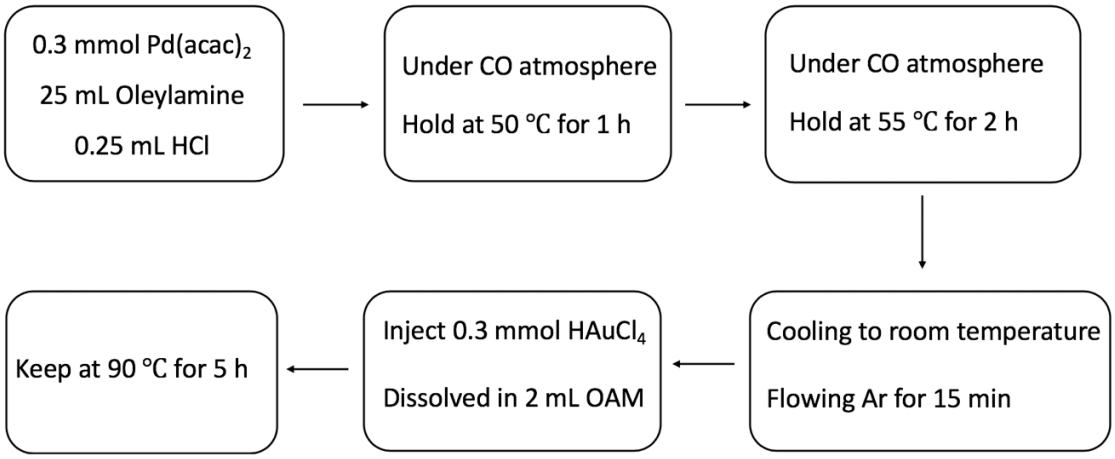

Figure 2.4 Schematic illustration of synthetic route for gold doped palladium nanosheets (Au@Pd NSs 2).

Au@Pd NSs were also synthesized through one pot synthesis, where Pd nanosheets were synthesized first through the method mentioned above, with Au metal precursors added later. To successfully grow gold on the palladium nanosheets, controlling temperature, time and inert gas atmosphere is very important. In the case of high temperature or long synthesis time, either the nanosheets would break, or there will be Au nanoparticles generate. Short time would lead to the

failure of growing and the remaining CO gas from the nanosheet synthesis step would trigger the rapid reduction of gold, along with nanoparticle agglomeration. Based on a series of trial, growing Au on the Pd NSs 2 was succeed and had the best morphology. The method is as following: after the synthesis of Pd NSs 2, naturally cool down the solution to the room temperature and stop purging the CO gas into the system, flowing Ar into the sealed four-neck flask for at least 15 minutes to blow away the remaining CO in the solution. Hydrogen tetrachloroaurate hydrate (0.3 mmol, 102 mg) dissolved in 2 mL Oleylamine was injected, and then the temperature was raised to 90 ℃. After 2-hour reaction, Au@Pd NSs 2 was collected using the same centrifugal washing method. The final product was dispersed in 10 mL hexane.

2.1.5 Post-synthesis treatment

After the organic solvothermal synthesis, the as synthesis nanosheets were loaded on carbon for further electrochemical tests. 15 mg Tanaka carbon and 20 mL toluene were added into a centrifuge tube with 50 mL capacity and ultra-sonication for 5 minutes. Then the palladium nanosheets dispersed in hexane were added and continue to be diluted with hexane till reaching the maximum capacity. In order to make the nanosheets more evenly distributed on carbon, the solution was further ultra-sonicated for at least 30 minuets until there is no precipitation at the tube bottom. The suspension was centrifuged at 10,000 rpm for 5 minutes to precipitate out the Pd nanosheets loaded on carbon. The collected product was re-dispersed and sonicated in 50 mL hexane, centrifuged at 10,000 rpm for 5 minutes. This procedure has been repeated for three times. The final Pd NSs/C and Au@Pd NSs/C catalyst were collected by vacuum dry, annealing at 185℃ overnight to clean the organic surfactant, and stored for future test.

2.2 Material characterization

FEI Tecnai 12 microscope operated at 100 kV was used to acquire Transmission Electron Microscopy (TEM) images of palladium-based nanosheets. The referred high resolution TEM (HRTEM) images were acquired with Jeol Grand ARM aberration corrected Transmission Electron Microscopy. Inductively Coupled plasma mass spectrometry (ICP-MS) was performed on a PerkinElmer Elan DRC II Quadrupole. An Oxford Xmax 100TLE windowless X-ray detector was used to collect the energy dispersive spectra (EDS).

2.2.1 Transmission Electron Microscopy (TEM)

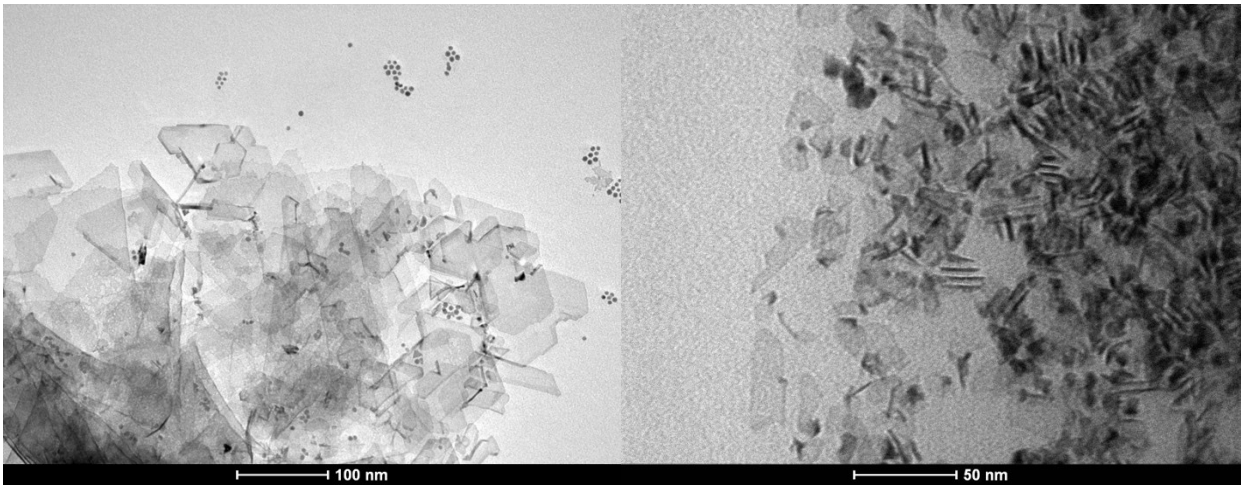

Figure 2.5 TEM images of Pd NSs1.

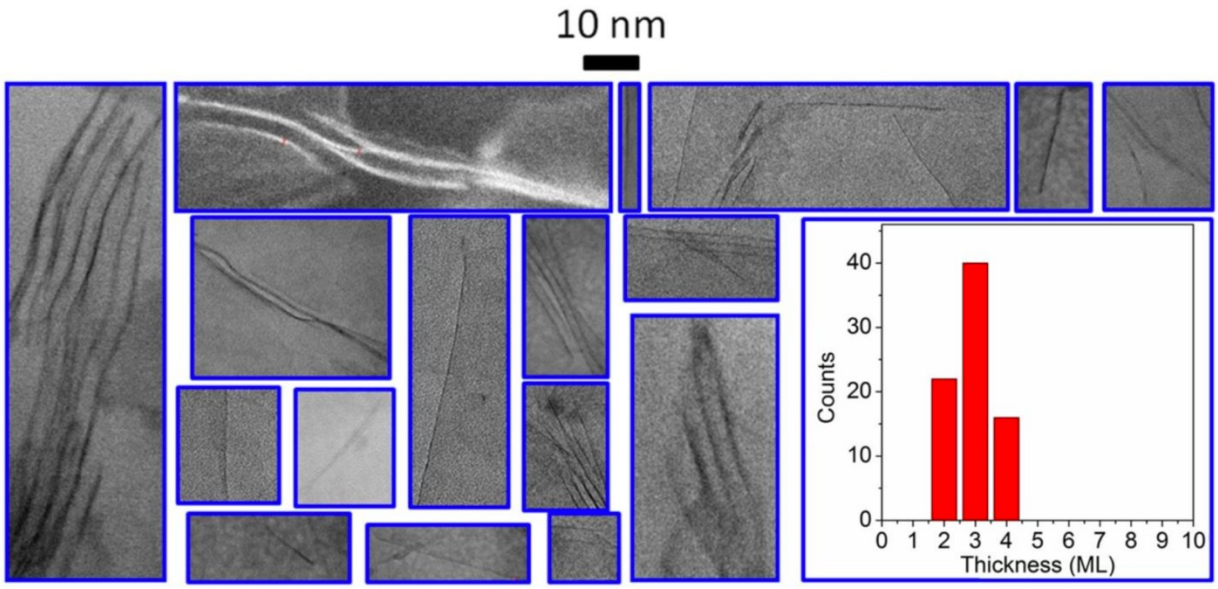

Figure 2.6 TEM images of Pd NSs with an average thickness of 3 mL and the thickness distribution. Adapted with permission from ref[9]. Copyright 2019 Science.

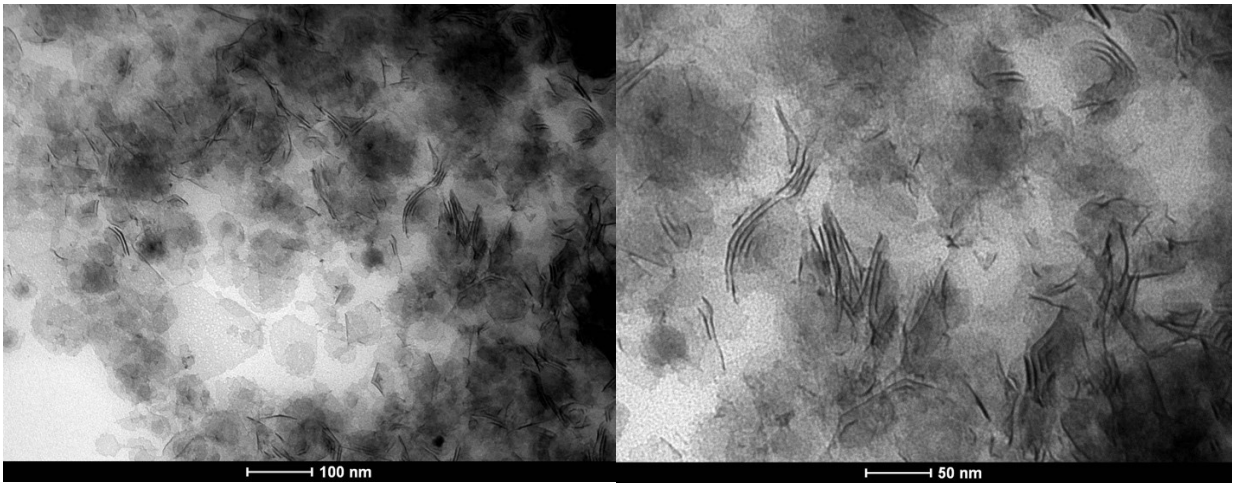

Figure 2.7 TEM images of Pd NSs 2.

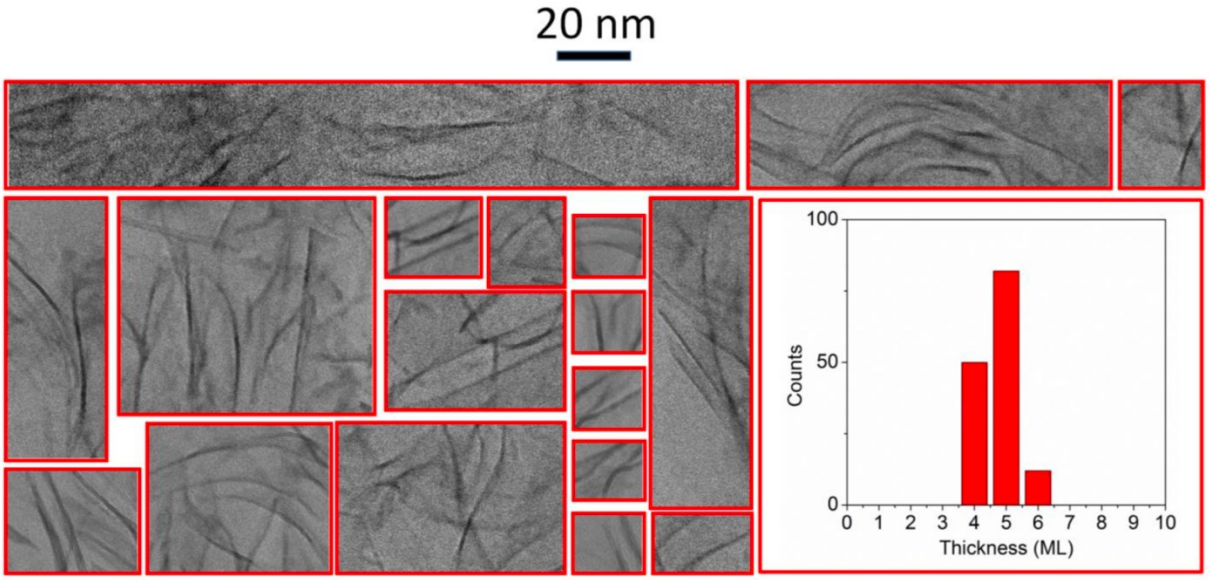

Figure 2.8 TEM images of Pd NSs with an average thickness of 5 mL and the thickness distribution. Adapted with permission from ref[9]. Copyright 2019 Science.

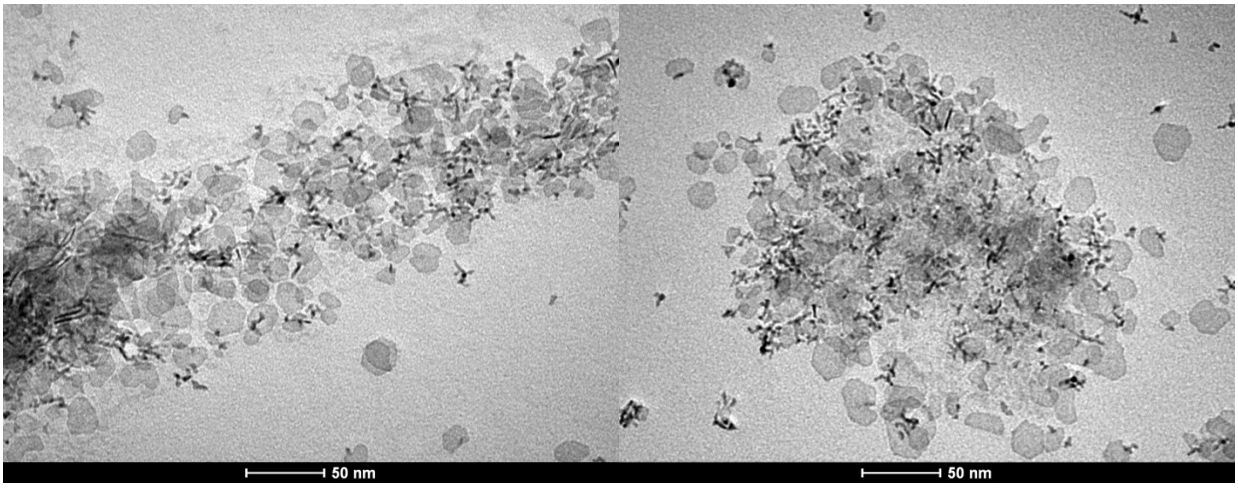

Figure 2.9 TEM images of Pd NSs 3.

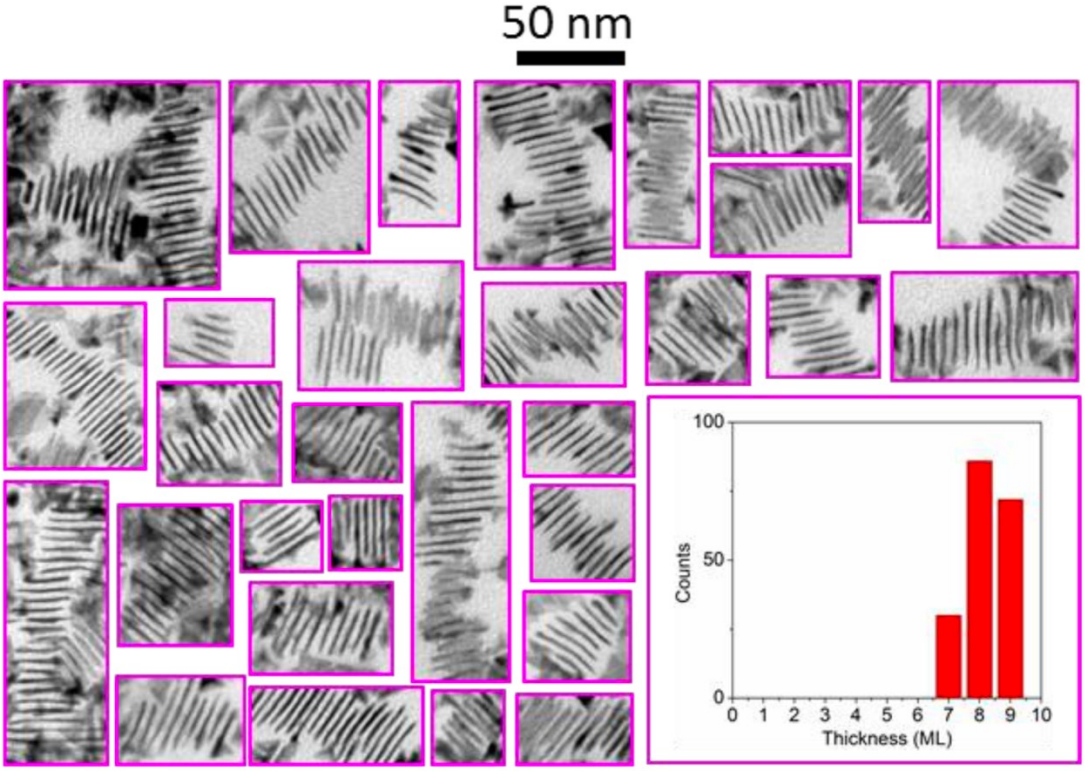

Figure 2.10 TEM images of Pd NSs with an average thickness of 8 mL and the thickness distribution. Adapted with permission from ref[9]. Copyright 2019 Science.

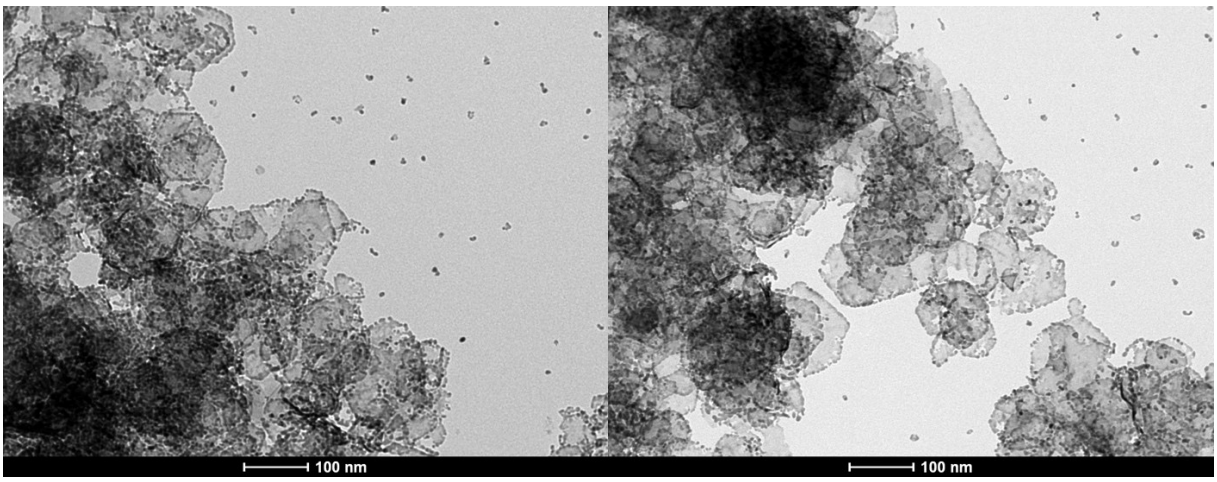

Figure 2.11 TEM images of Au@Pd NSs 2.

The TEM images of Pd NSs before loading on the carbon have been showed in Figure 2.5 to Figure 2.11. As shown, Pd NSs 1, 2, 3 have the corresponding edge lengths of 100 to 260 nm, 50 to 150 nm, and ~ 20 nm, respectively. The thickness of the nanosheets was confirmed based on the previous published research work in our lab as shown in Fig 2.6, Fig 2.8 and Fig 2.10: exhibiting thickness of 3 ± 1ML, 5 ± 1ML and 8 ± 1ML correspondingly (± represents standard deviations). Some small nanoparticles were generated during the synthesis of Pd NSs 1, due to the sudden unstable temperature. As shown in Fig 2.11, gold has been successfully growing on the Pd NSs 2, particularly distinct on the edge of nanosheets. Though a small part of nanosheets broke due to long time synthesis, the overall quality is acceptable.

2.2.2 High Resolution Transmission Electron Microscopy (HRTEM)

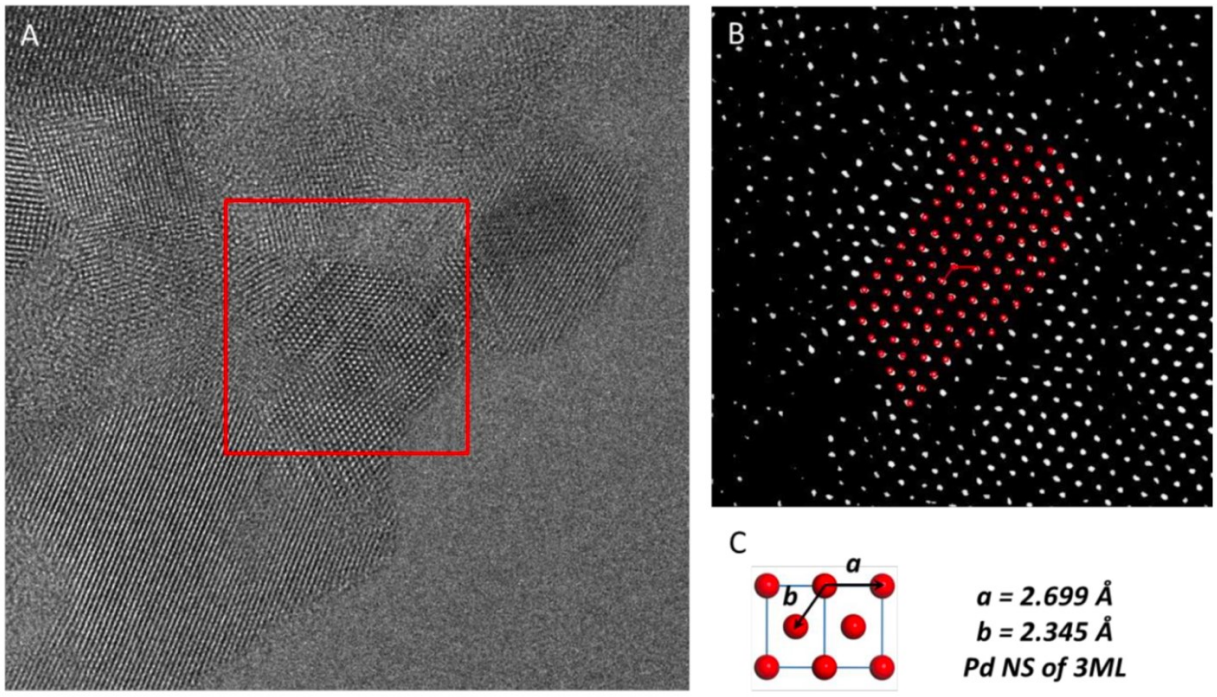

Figure 2.12 (A) HRTEM images of Pd NSs 1, the marked area was used to calculate the lattice parameters. (B) the calculated average two-dimensional lattice is shown in red circles, overlapping with the atom intensity peak positions of the Pd NSs. (C) the unit vectors of the average lattice, for which a and b are in $[\bar{1}10]$ and $[1\bar{1}2]$ direction respectively. Adapted with permission from ref[9]. Copyright 2019 Science.

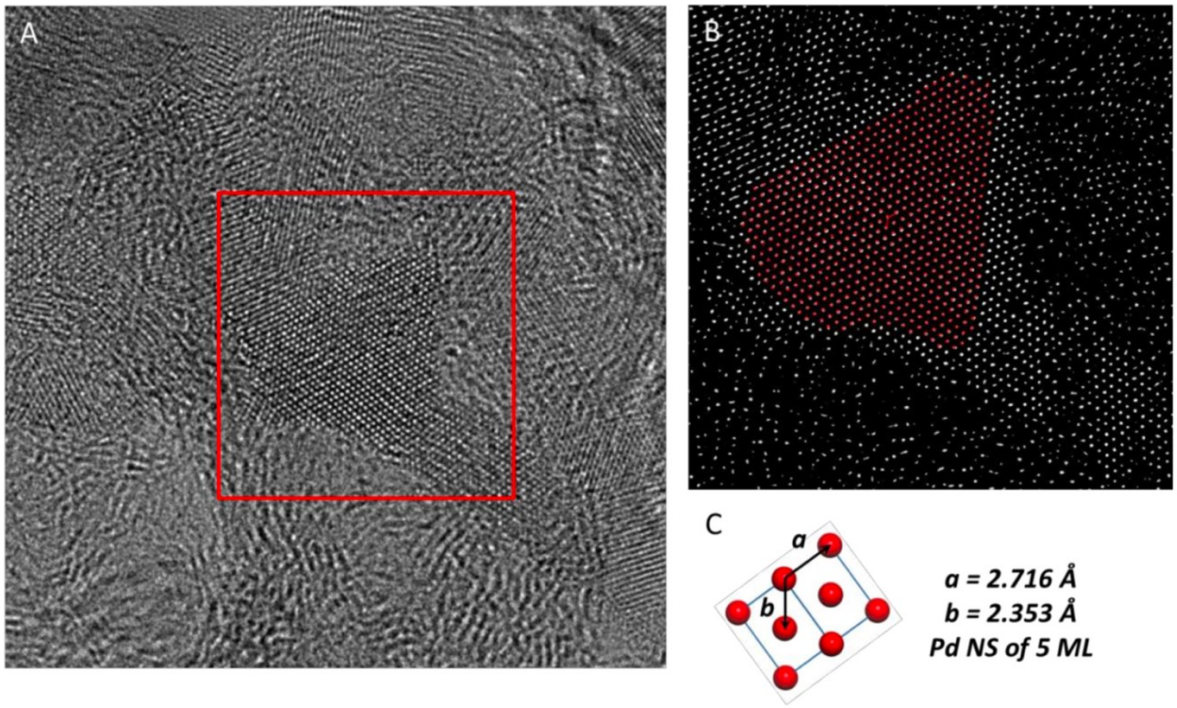

Figure 2.13 (A) HRTEM images of Pd NSs 2, the marked area was used to calculate the lattice parameters. (B) the calculated average two-dimensional lattice is shown in red circles, overlapping with the atom intensity peak positions of the Pd NSs. (C) the unit vectors of the average lattice, for which a and b are in $[\bar{1}10]$ and $[1\bar{1}2]$ direction respectively. Adapted with permission from ref[9]. Copyright 2019 Science.

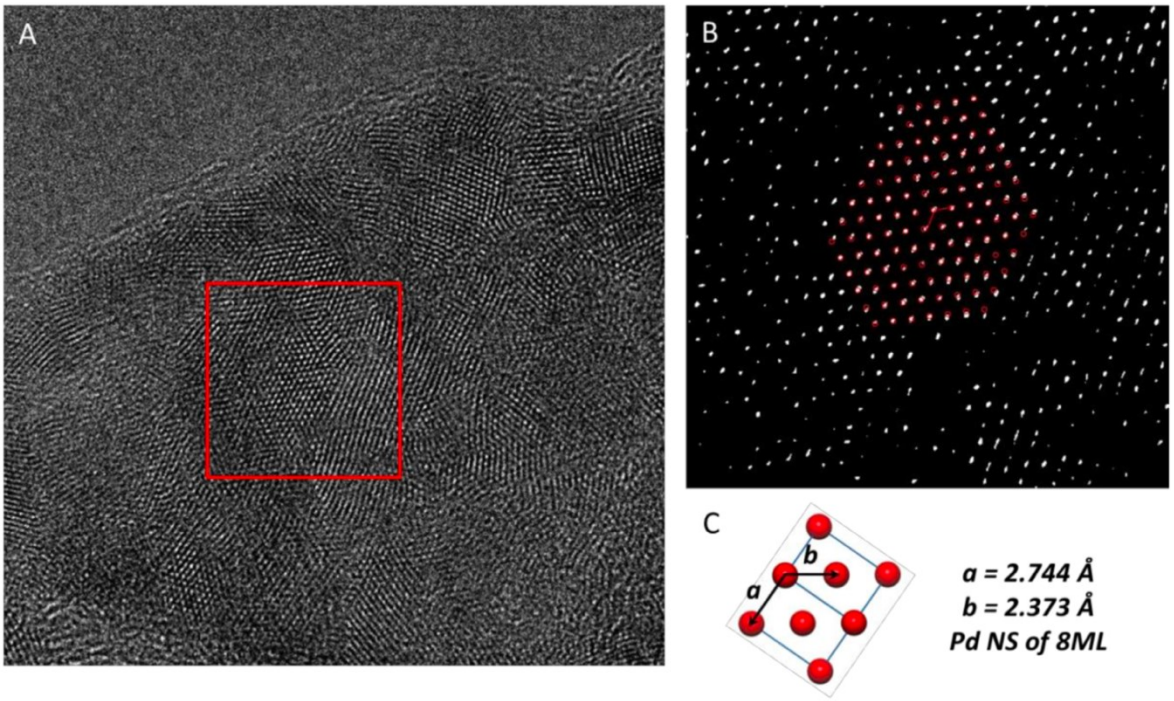

Figure 2.14 (A) HRTEM images of Pd NSs 3, the marked area was used to calculate the lattice parameters. (B) the calculated average two-dimensional lattice is shown in red circles, overlapping with the atom intensity peak positions of the Pd NSs. (C) the unit vectors of the average lattice, for which a and b are in $[\bar{1}10]$ and $[1\bar{1}2]$ direction respectively. Adapted with permission from ref[9]. Copyright 2019 Science.

Base on the previous published research work in our lab, the as synthesized Pd nanosheets adopted a [110] basal plane. The HRTEM images and corresponding lattice parameters are shown in Fig 2.12 to 2.14. The lattice parameters of Pd NSs 1 were determined to be a = 0.270 nm, b = 0.235 nm, with an angle of 124.7° between them, which correspond to the unit vectors along the norm vector of $[\bar{1}10]$ and $[1\bar{1}2]$ planes projected along the [110] orientation of the fcc Pd lattice. The parameters were measured to be a = 0.272 nm, b = 0.235 nm for Pd NSs 2, and a = 0.274 nm, b = 0.237 nm for Pd NSs 3. Compared with bulk value (a = 0.275, b = 0.238), all Pd NSs displayed

compressive strain to different extents. There is a clear trend that the compressive strain increases as the thickness of nanosheets decreases.

2.2.3 Inductively Coupled Plasma Mass Spectroscopy (ICP-MS)

The ICP samples were prepared after the nanosheets loaded on carbon. 1 mg of each Pd NSs/C and commercial Pd/C (10%) were weighed out and dissolved in 5 mL Aqua Regia overnight. The solutions were diluted 50 times with DI water and filtered by PTFE hydrophilic filter membrane. Before the nanosheet samples test, standard palladium calibration curve was obtained (seen in Fig. 2.15). Based on the calculation, the Pd loadings are confirmed (Table 2.2), the loadings of Pd NSs 1, NSs 2 and NSs 3 are 35.91%, 24.26% and 18.19% separately. The loading of commercial Pd/C is 10.06%, indicating the results is relatively precise.

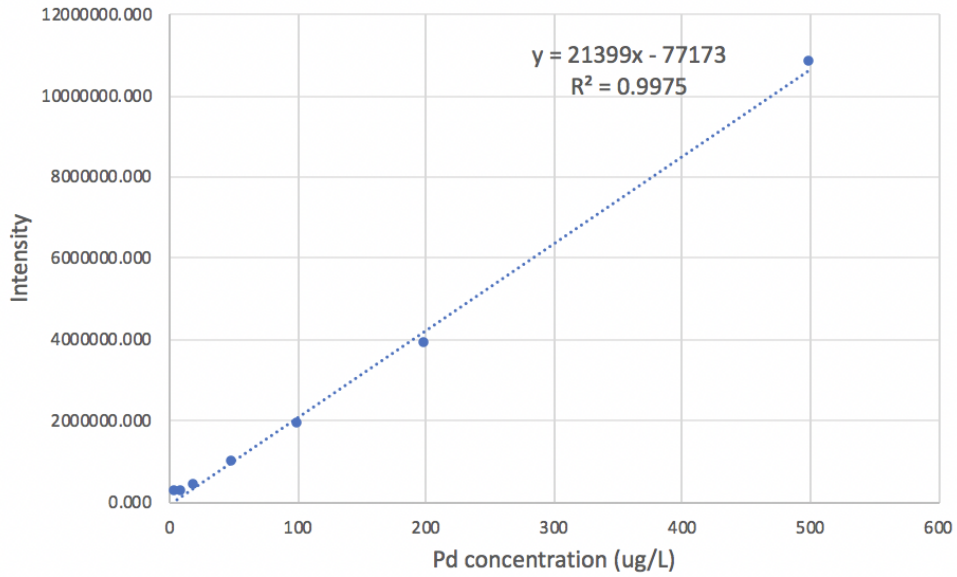

Figure 2.15 Calibration curve of Pd concentration.

Table 2.2 Pd loading of catalyst based on ICP test.

Catalysts	Pd loading (%)
Pd NSs 1/C	35.91
Pd NSs 2/C	24.26
Pd NSs 3/C	18.19
Commercial Pd/C	10.06

2.2.4 Energy Dispersive X-ray Spectrometry (EDS).

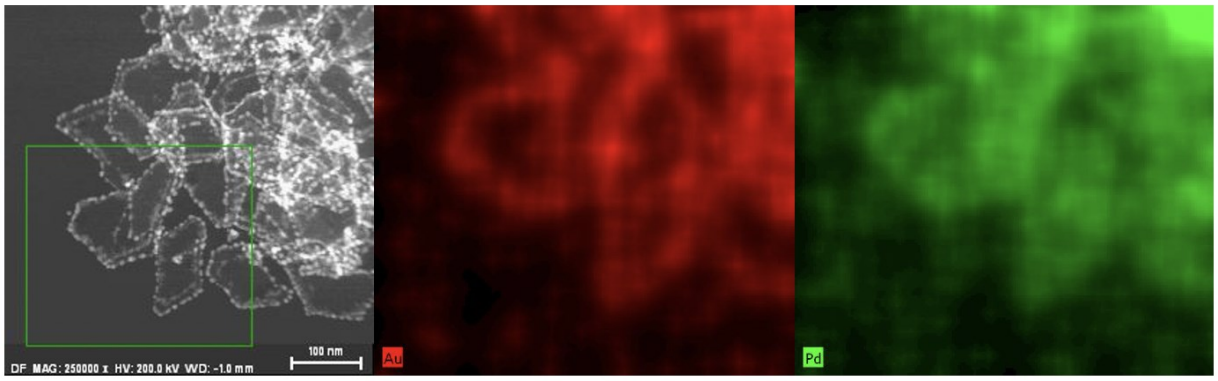

Figure 2.16 Element mapping for Au@Pd NSs 2.

From the results of element mapping through Energy Dispersive X-ray Spectrometry, most of Au has grown on the edge of the Pd NSs 2.

2.3 Electrochemical test

2.3.1 Formic acid oxidation reaction

A Metrohm PGSTAT302N potentiostat was used for the electrochemical studies of formic acid oxidation reaction (FAOR). A 5 mm diameter glassy carbon rotating disk electrode was used as the working electrode. Ag/AgCl redox couple and Pt wire were used as reference and counter electrode respectively. The schematic and real experimental test setup is showed in Fig 2.17 and Fig 2.18. For working electrode preparation, the Pd NSs/C catalysts were dispersed in aqueous solution containing 10% IPA and 0.025% Nafion, with concentration of 1 mg/mL. The mixture is ultrasonicated for 30 minutes to form homogeneous catalyst ink. Then 20 uL ink was dripped onto the glassy carbon surface and dried in air (see in Figure 2.19).

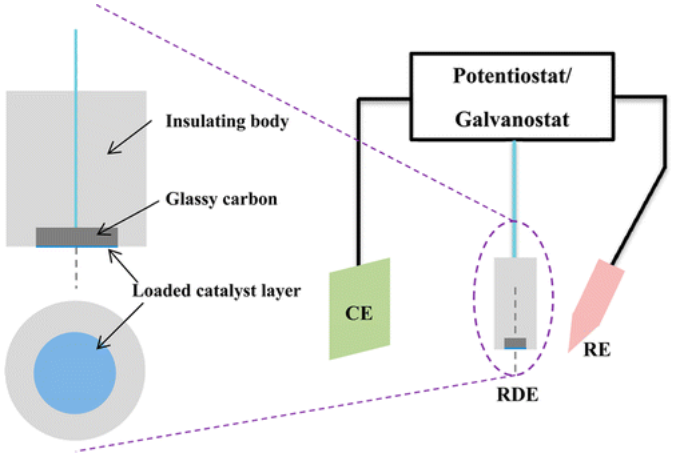

Figure 2.17 Schematic diagram of typical rotating-disk electrode (RDE) testing setup in three electrode configurations. Adapted with permission from ref [26]. Copyright 2015 American Chemical Society.

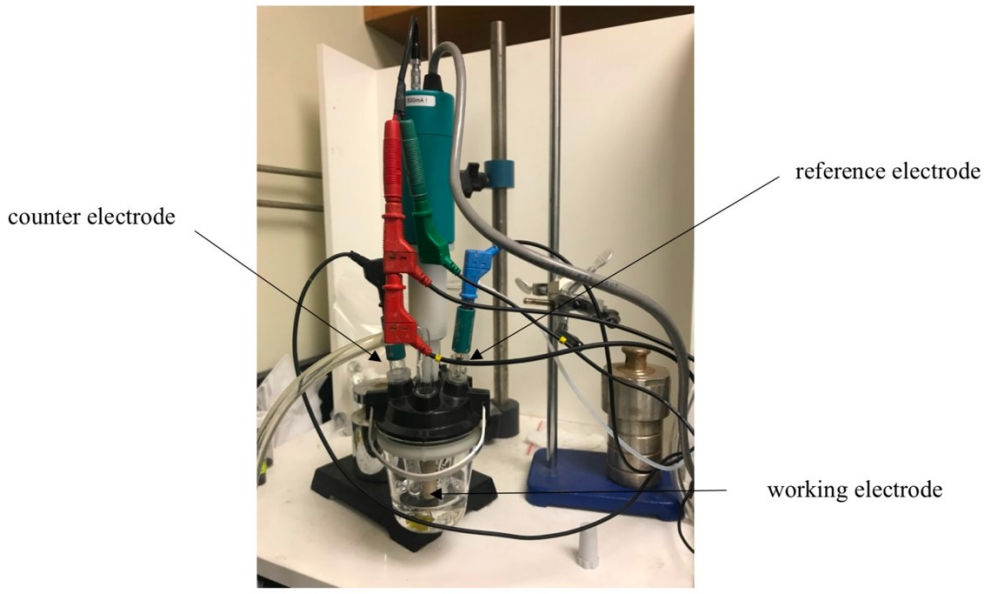

Figure 2.18 Photo of experimental setup for formic acid oxidation electrochemical test.

Figure 2.19 Photo of glassy carbon electrode with catalysts.

Cyclic voltammogram (CV), formic acid oxidation reaction (FAOR) curve and CO stripping curves were recorded at the scan rate of 50 mV/s. For CV and CO stripping, 0.1 M

perchloric acid $HClO_4$ was used as electrolyte. Under Argon saturated condition, CV was recorded between the potential range 0.00-1.00 V vs.RHE for 20 cycles to clean the working electrode surface. CO stripping test was conducted before the FAOR activity test, to analyze the CO binding energy of the catalyst. The specific testing protocol for CO stripping is as following: CO gas was flow into the cell for 8 minutes, during which CO will cover the whole catalyst surface. Then Argon was introduced to blow away the remaining CO which has not combined with the catalysts in the test system. Then a CV scan ranging from 0 to 1.2 V vs.RHE was conducted to oxidize the CO on the electrode surface in an Ar- saturated condition. FAOR activity and stability tests were carried in electrolyte of 0.1 M $HClO_4$ and 0.5 M HCOOH, with scan range 0.00-1.00 V vs.RHE.

2.3.2 CO_2 reduction reaction

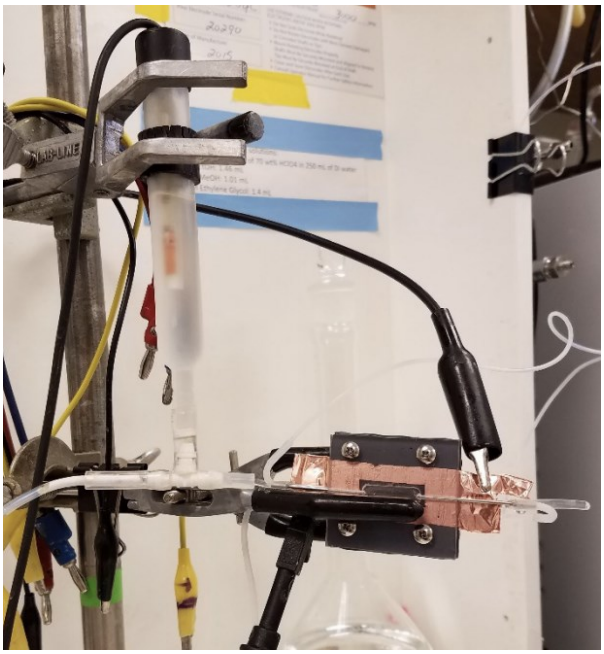

Figure 2.20 Photo of experimental setup for CO_2 reduction electrochemical test.

The electrocatalytic studies of CO_2 reduction were performed with a gas diffusion cell and an Autolab 302 potentiostat (Metrohm). An experimental set up of the cell is shown in Fig 2.20. Three electrode system was applied, with $Hg/HgSO_4$ electrode and IrO_2 on gas diffusion layer

(GDL) as reference and counter electrode, respectively. The working electrode was Pd NSs deposited on GDL. Pd NSs 2 and Au@Pd NSs 2 working electrodes have been prepared as the following protocol: 15 mg catalysts were dispersed in 10 mL isopropyl alcohol (IPA) and 75 uL Nafion. The IPA was used to disperse the catalyst while the function of Nafion is attaching the catalyst to the GDL. After ultrasonicated for 30 minutes to get a homogeneous catalyst ink, 3 mL of the catalyst ink was dripped onto the GDL and dried on the hotplate. The loading is approximately 2 mg/cm^2. Catalysts loaded on gas diffusion layer is showed in Fig 2.21. The IrO_2 counter electrode has also been made in similar way, with each counter electrode having the IrO_2 loading of 5 mg per GDL.

1 M $KHCO_3$ was used as electrolyte, flowing through both cathodic and anodic compartments of the cell, which was separated by an anion exchange membrane, at 0.5 mL/min by using a syringe pump. CO_2 gas was introduced to the cathode chamber at a constant flow rate of 20 sccm. At the beginning of the test, the resistance between the cathode and reference electrode was measured. Cyclic voltammogram (CV) was recorded at the potential range between 0-1 V vs.RHE at scan rate of 50 mV/s. After 3 cycles for the surface cleaning purpose, each sample was tested chronoamperometry at 0.00, -0.05, -0.10, -0.15, -0.20, -0.25, -0.30 V vs RHE separately for 12 minutes, during which the CO_2 reduction current was recoded. After each specific potential chronoamperometry test, a CV scan was followed to remove the possible adsorbed product CO. The gas phase products were measured online through gas chromatograph-mass spectrometry (GC-MS). Liquid phase products were collected and analyzed using the nuclear magnetic resonance (NMR) spectroscopy. After the electrochemical test finished, all the gas diffusion layers were collected and dissolved in Aqua Regia, which would be further analyzed by ICP test to verify the metal mass.

The faradaic efficiency towards specific gas or liquid product was calculated based on the following formula:

$$\text{FE}\ (\%) = \frac{I\ gas\ product}{I\ total} = \frac{gas\ flow\ rate \times \frac{P}{R \times T} \times F \times n \times gas\ product\ concentration}{Average\ total\ current} \times\ 100\ \%$$

$$\text{FE}\ (\%) = \frac{I\ liquid\ product}{I\ total} = \frac{liquid\ flow\ rate \times F \times n \times liquid\ product\ concentration}{Average\ total\ current} \times\ 100\ \%$$

Where P is the atmospheric pressure, R is the idea gas constant, T is the room temperature, F is the Faraday constant and n is the number of electrons transferred for each molecule produced.

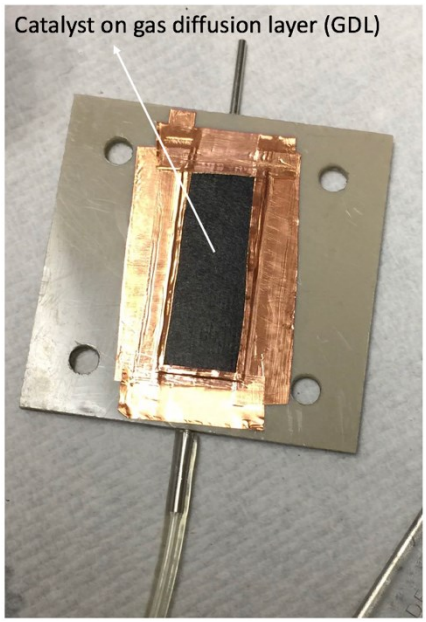

Figure 2.21 Photo of working electrode for CO_2 electrochemical reduction test.

3. Results and discussion

3.1 Formic acid oxidation reaction

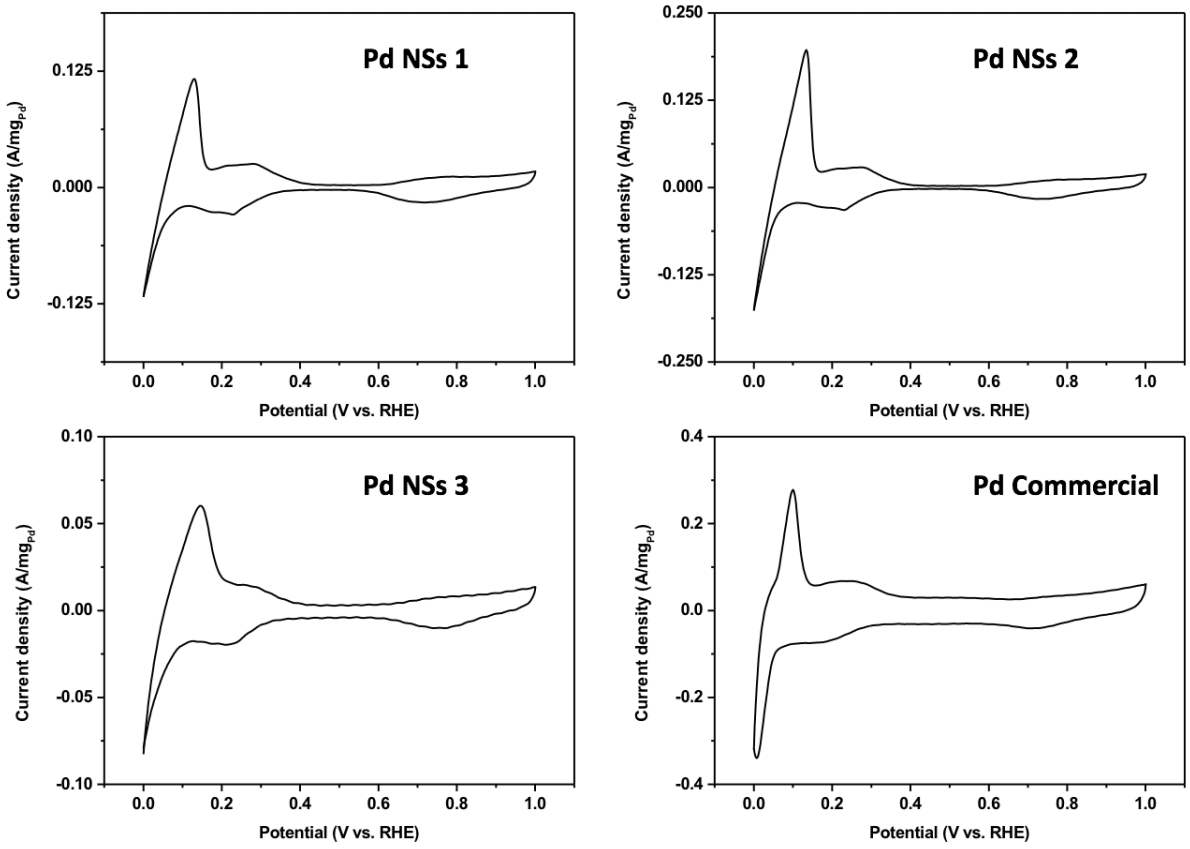

Figure 3.1 Cyclic voltammogram curves of Pd NSs and Pd commercial recorded in Ar-saturated 0.1 M $HClO_4$ at 50 mV s^{-1}.

Figure 3.1 shows typical CV curves of as-prepared Pd NSs/C in comparison to the commercial Pd/C in Ar-saturated 0.1 M $HClO_4$ at the scan rate of 50 mV s^{-1}. All display distinct potential region related to the H_{upd} adsorption/desorption process ($H^+ + e^- = H_{upd}$) from 0 to 0.4 V and the formation of OH_{ad} layer ($2H_2O = OH_{ad} + H_3O^+ + e^-$) beyond 0.6 V, where the H_{upd} and

OH_{ad} represent the under potential deposited hydrogen and the adsorbed hydroxyl group respectively[27]. During the backward scan, a reduction peak of palladium oxide could be observed in the potential range 0.6 to 0.8 V.

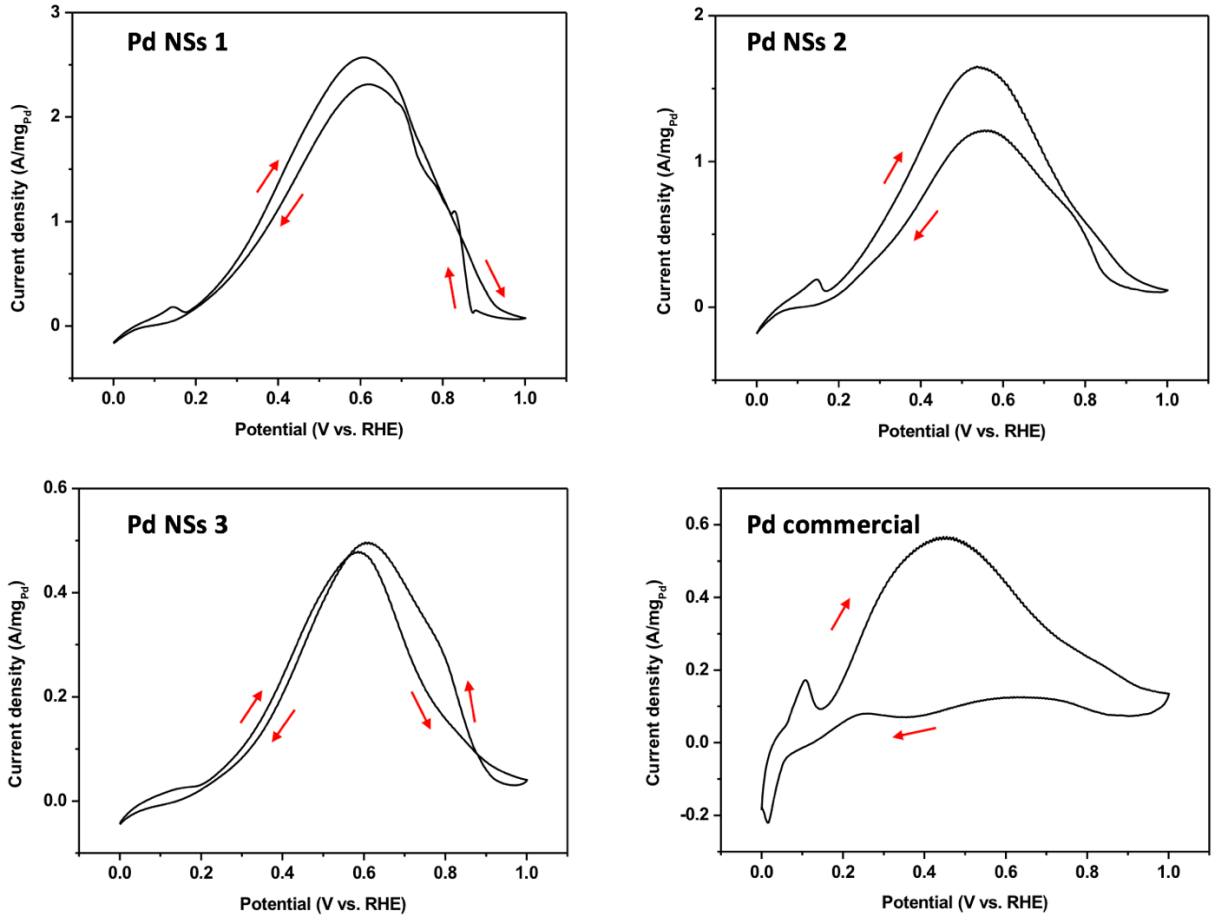

Figure 3.2 First cyclic voltammogram scan curves of Pd NSs and Pd commercial recorded in Ar-saturated 0.1 M $HClO_4$ + 0.5 M HCOOH at 50 mV s^{-1}.

Figure 3.2 displays the first cycle of mass normalized CVs for Pd NSs and Pd commercial in 0.1 M $HClO_4$ + 0.5 M HCOOH solution at a scan rate of 50 mV s^{-1}. At the potential lower than 0.2 V, the peaks corresponding to the H_{upd} adsorption/desorption are still observed in the presence of formic acid. Distinct anodic peaks at potential high than 0.4 V are attributed to the oxidation of

formic acid. During the backward scan, the peak is assigned to the oxidation of formic acid on the newly reduced Pd surface. Pd NSs 3 exhibited a dissimilar performance when compared with others: its cathodic scan current density is partially higher than that of anodic scan. One possible explanation is CO poisoning: in the anodic scan, the oxidation of formic acid on Pd NSs 3 surface may go through an indirect pathway, during which the CO intermediates are generated binding to the active sites that originally to be combined with formic acid, thereby decreasing the catalytic activity. Then as the applied potential increases, CO is further oxidized, releasing those active sites for catalyzing the formic acid oxidation, so that the backward current density cranked up. It could also be due to the electrosorption of OH^- : the OH^- ion is also a poison for formic acid oxidation, as it most likely blocks the adjacent vacant surface sites needed for the decomposition of formate (an intermediate in the oxidation process) to CO_2[28].

The stability of electrocatalyst has been considered one of the most important issue to be addressed for the commercialization of practical fuel cell[27]. Preliminary stability tests were performed by applying a cycling potential between 0 and 1 V for 20 cycles. Figure 3.3 shows comparative stability test results of electrodes prepared from Pd NSs and commercial Pd. By comparing the peak current density retention in the forward sweep after 20 cycles, it can be clearly seen that the catalytic performance of Pd commercial catalyst rapidly decreases, with only 13.53% current retention (see Table 3.1). Whether during the 1st cycle or the 20th cycle, the retrace current peak of Pd commercial is much weaker compared with that of Pd NSs, indicating the redox reactions on the surface of commercial Pd has already caused inactivation of its catalytic activity. A substantially improved stability are demonstrated by Pd NSs 1 and Pd NSs 2, with 85.89% and 77.55% current retention respectively. The active sites poisoning phenomenon of Pd NSs 3 gradually disappears during the cycling as shown in Fig 3.3: in the 20th cycling curve, the anodic

scan current density exceeds that of cathodic scan, with an augment in the forward current density from 1st to 20th cycle. This may due to the surface reconstruction of Pd NSs 3 during the cycling, so that the reaction pathway and the binding states with the intermediates are change in a direction more conducive to the formic acid oxidation.

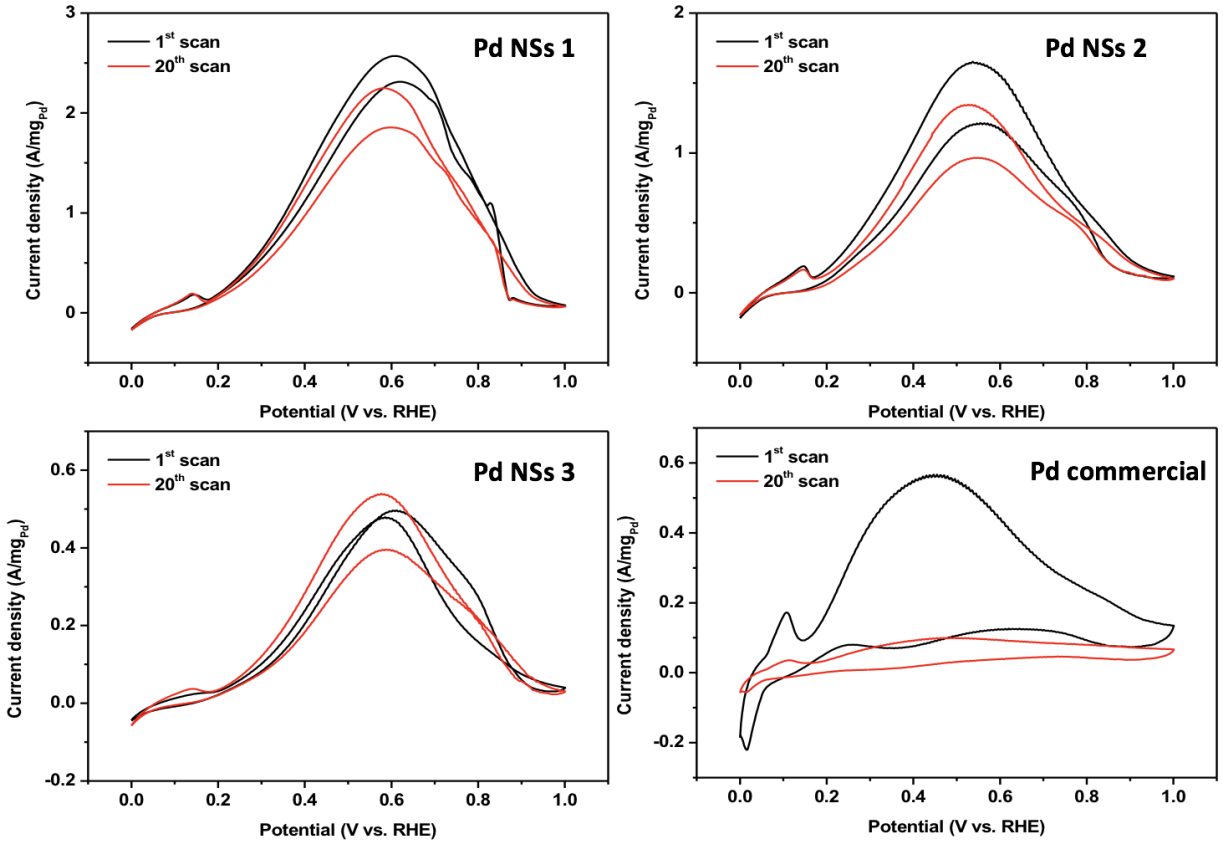

Figure 3.3 Comparison of faor catalytic performance between 1st and 20th cycle recorded in Ar-saturated 0.1 M $HClO_4$ + 0.5 M HCOOH at 50 mV s^{-1}.

Table 3.1 Stability of the catalysts in terms of the peak current retention in the forward sweep.

Catalysts	Retention of peak current (%)
Pd NSs1	85.89
Pd NSs2	77.55
Pd NSs 3	112.76
Pd Commercial	13.53

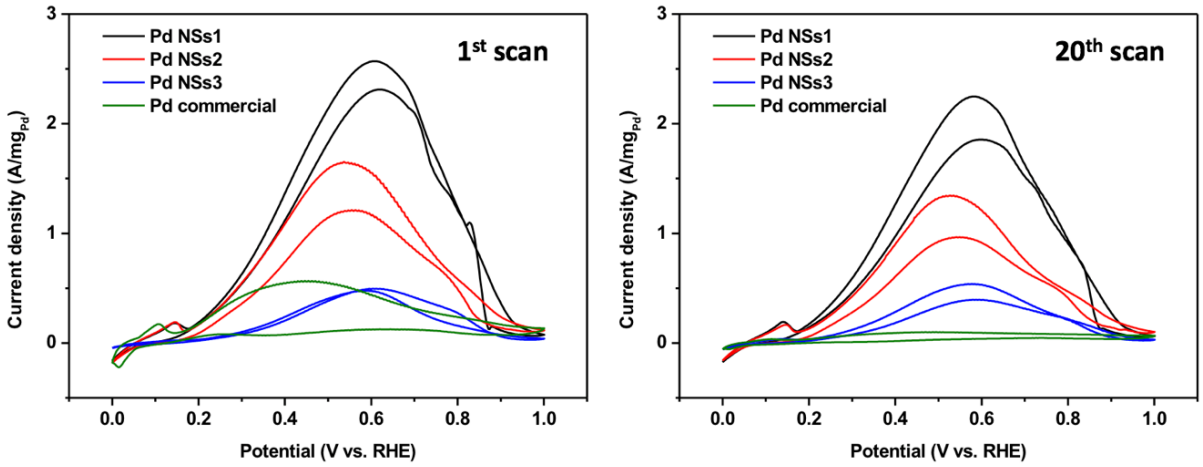

Figure 3.4 Comparison of the faor performance between Pd NSs and Pd commercial in the 1st and 20th cycle.

Figure 3.4 displays FAOR electrocatalytic performance comparison among Pd NSs and Pd commercial in the 1st and 20th cycle respectively. The specific peak potential and corresponding peak mass activity are listed in table 3.2. In terms of peak mass activity, all Pd nanosheets demonstrate comparable or better performance than Pd commercial. As intuitively shown in Figure

3.5, Pd NSs 1 exhibits an especially high peak current density of 2.57 A/mg_{Pd} in the first cycle, followed by Pd NSs 2 with peak mass activity of 1.652 A/mg_{Pd}, almost 5 times and 3 times that of commercial catalyst (0.567 A/mg_{Pd}) respectively. Due to the initial poisoning of the active sites, the mass activity of Pd NSs 3 at the beginning is slightly lower than that of Pd commercial. After 20 cycles, all Pd NSs have higher catalytic activity than the commercial one and follow the order of Pd NSs 1 > Pd NSs 2 > Pd NSs 3 > Pd commercial. Though the peak potential of all nanosheets are higher than Pd commercial, the mass activity of Pd NSs 1 and Pd NSs 2 exceed that of the commercial one almost in all applied potential range. All the peak potential of nanosheets are negatively shifted after 20 cycles, indicating that the FAOR occurs more and more favorably. Form a sharp contrast with Pd commercial, the peak potential of which positively shifts after cycling.

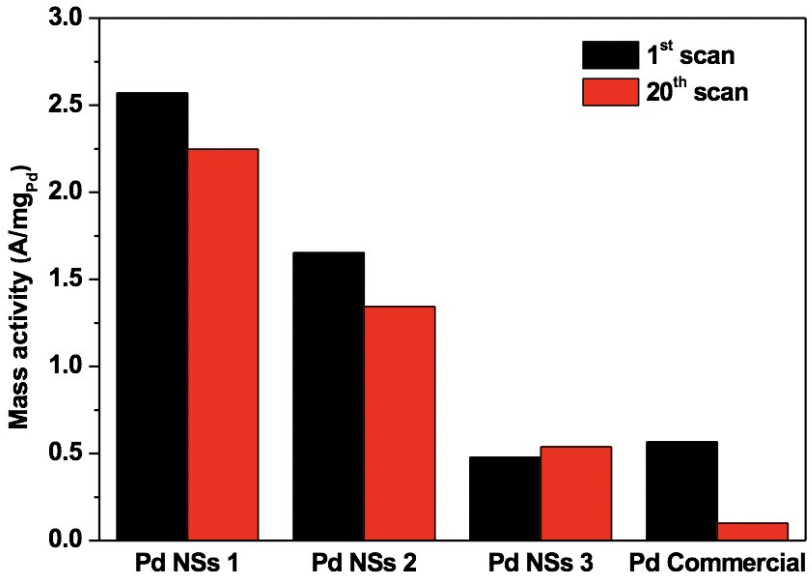

Figure 3.5 Comparison of peak mass activity towards FAOR.

Table 3.2 Peak potential and corresponding mass activity of Pd based catalysts towards FAOR.

Catalysts	1st scan		20th scan	
	Peak potential (V vs. RHE)	Mass activity (A/mg_{Pd})	Peak potential (V vs. RHE)	Mass activity (A/mg_{Pd})
Pd NS1	0.605	2.570	0.583	2.247
Pd NS2	0.537	1.652	0.534	1.344
Pd NS3	0.586	0.479	0.576	0.539
Pd Commercial	0.454	0.567	0.486	0.100

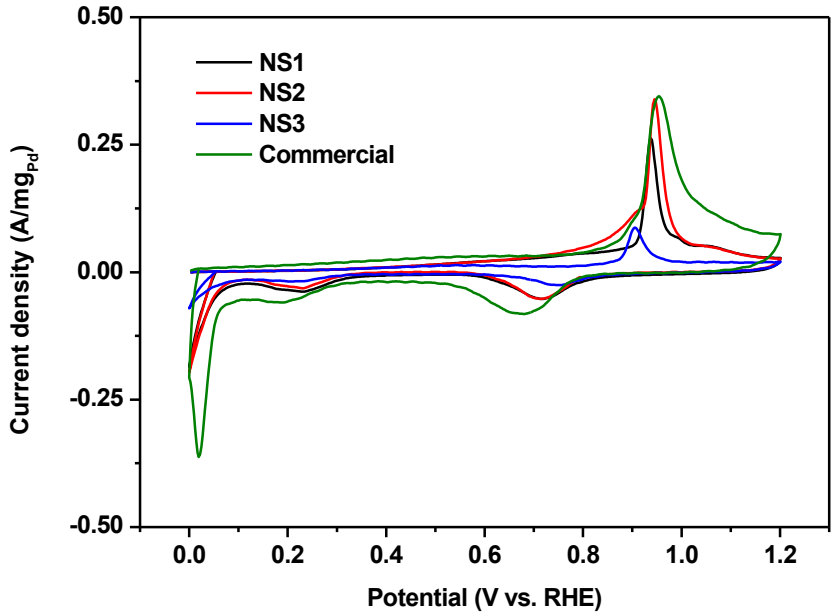

Figure 3.6 CO stripping curves of Pd NSs and Pd commercial recorded in 0.1 M $HClO_4$.

As revealed by CO stripping curves (Figure 3.6), the peak potential of CO oxidation on Pd nanosheets all negatively shift and follow the order of Pd NSs 3 < Pd NSs 1 < Pd NSs 2 < Pd Commercial, manifesting that Pd nanosheets possess better CO intermediate tolerance capacity. If only compare the onset potential of CO oxidation, Pd NSs 2 also shows more tolerance to the CO poisoning.

As a demonstration, the Pd nanosheets with different thickness and in-plane compressive strain could serve as efficient electrocatalysts towards formic acid oxidation with higher mass activity, stability and CO tolerance than the Pd commercial. The improved performance could be rationally ascribed to the unique two-dimensional structure and strain effect.

3.2 CO_2 reduction reaction

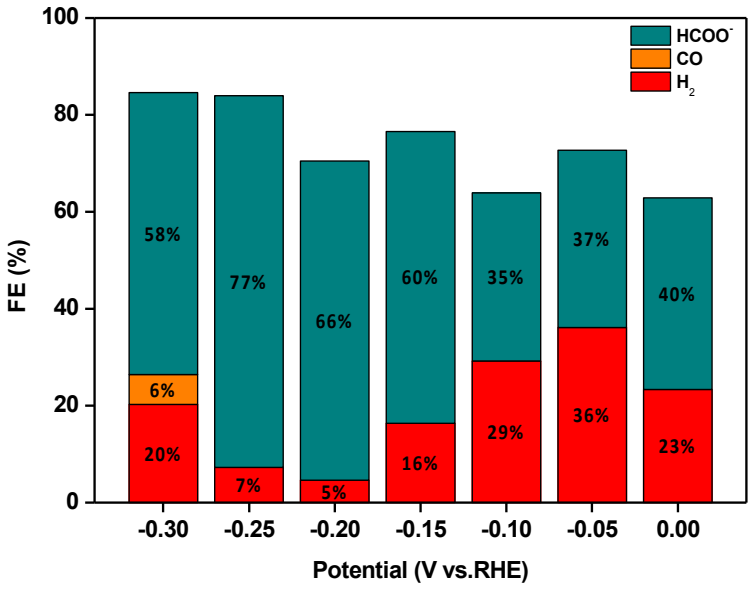

Figure 3.7 Faradaic efficiency towards formate, carbon monoxide and hydrogen on Pd NSs 2.

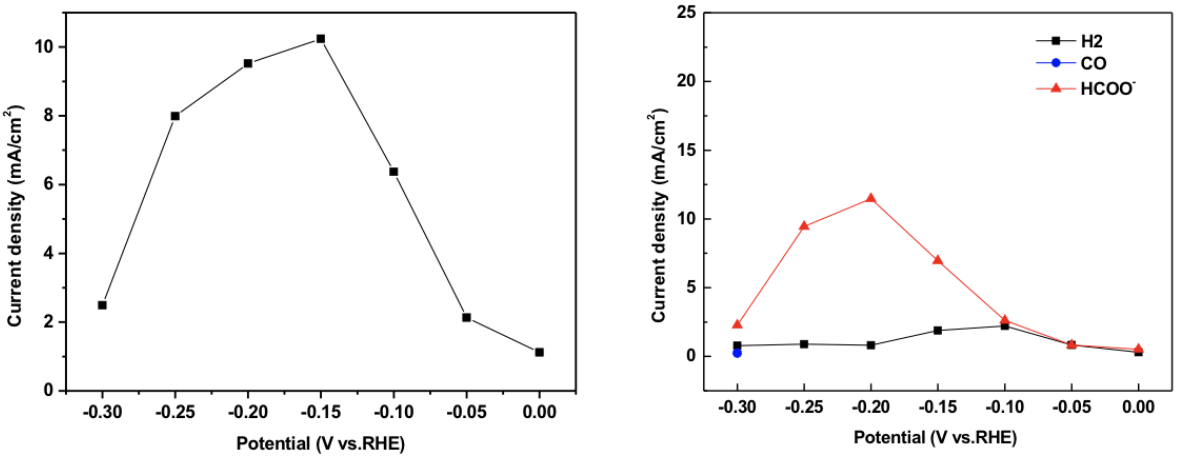

Figure 3.8 Geometric current density at the 300th second (left), partial current density for specific product (right) on Pd NSs 2.

For the CO_2 electrochemical reduction, Pd NSs 2 was pretested first since it has the highest yield and less nanoparticle formation during the synthesis process. Seven reduction potential points from 0 to -300 mV were choosen to conduct the chronoamperometry for 12 minutes. The faradaic efficiency distribution for specific reduction product on Pd NSs 2 are shown in Fig 3.7. The total faradaic efficiency (FE) of all detected products has not reached 100% due to the following reason: first, 5000 ppm standard calibration gas was diluted with argon using two mass flow controllers to form the gas product calibration curve. The result for the low concentration point could be imprecise due to the huge mass flow differences between the two controllers. Second, because of the low current density as shown in Fig 3.8 left, there may be errors in the FE calaculation process. Third, the not completely removed surface surfactant could also be responsible for the none-100% FE.

It can tell from the Fig 3.7, formate, hydrogen and crabon monoxide are the major product of CO_2 reduction on Pd NSs 2. The formation of formate is the dominant process at the beginning, and the selectivity towards the formate has an increasing tendency from 0 to -0.20 V as can be seen from the partial current density (Fig 3.8 right), which is due to the larger overpotential applied from a kinetics perspective. However, in the large overpotential range, the total current density (-0.15 to -0.30 V) as well as partical current density towards formate (-0.20 to -0.30 V) decreases. This fluctuation observed could be ascribed to different active phases and adsorption strength of reactants, intermediates and products. An possilbe explanation could be the transition of PdH_x active phases, phase one selectively reducing CO_2 to formate via the HCOO* intermediate while phase two selectively reducing redcuing CO_2 to CO via the COOH* intermediate[22]. In the potential range -0.15 to -0.25 V, CO* intermediates are gradually generated and quickly destroyed the PdH_x phase one. During this process the CO is still too hard to desorb from the surface due to the high CO binding energy, so that a decreasing in the current density appears. However, as the applied potential negatively shifts, the formation of the PdH_x phase two might be thermodynamically favorable, weaking the CO adsorption on the catalyst surface, so that CO is produced at high overpotential 300 mV.

To alleviate the poisoning effect mentioned above, gold has been grown on the Pd NSs 2. Since Pd is a strong CO-binding metal while Au is a weak CO-binding metal, ensemble effects like intermediate adsorption erergy change and energy barrier redcution might occur to favore the high selectivity as well as high activity. As illustrated in Fig 3.9, formate is the dominant reduction product (FE > 56%) in the low overpotential range (0.00 to -0.10 V), while CO is gradually become the main product from -0.15 to -0.3 V. Poisoning effect could still be observed intuitively in Fig 3.10 left, a clear decreasing of total current density between the potential from -0.15 to -0.25 V.

one possible explanation for this result could be: in the low overpotential range from 0 to -0.1 V, the formation of formate through Pd active sites is the dominant reaction, which also reflected in the augment of partial current density toward formate, as shown in Fig 3.10 right. As the applied potential negatively shifts, the larger overpotential enables Au to overcome the ernergy barrier starting producing CO, which strongly bond to the Pd active sites, decreasing the formation of formate. Therefore, in the large overpotential range (-0.15 to -0.30 V), CO production through Au dominates. In the potential range from -0.15 to -0.25 V, the generated CO intermdediates are adsorbed on the Pd surface. The appilded potential is not high enough to overcome the energy barrier of CO desorption to release all the CO. While at the potential of -0.30 V, the overpotential may be high enough to enable the fast generation and desorption of CO, so that there is an increasing of partial current density towards CO in Fig 3.10 right.

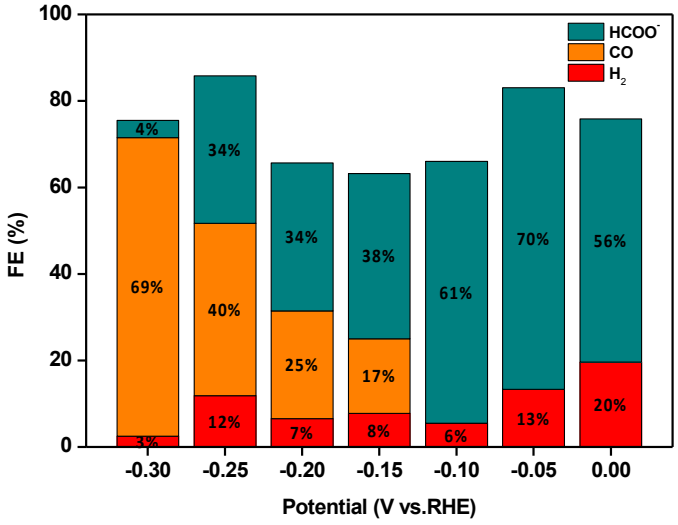

Figure 3.9 Faradaic efficiency towards formate, carbon monoxide and hydrogen on Au@Pd NSs 2.

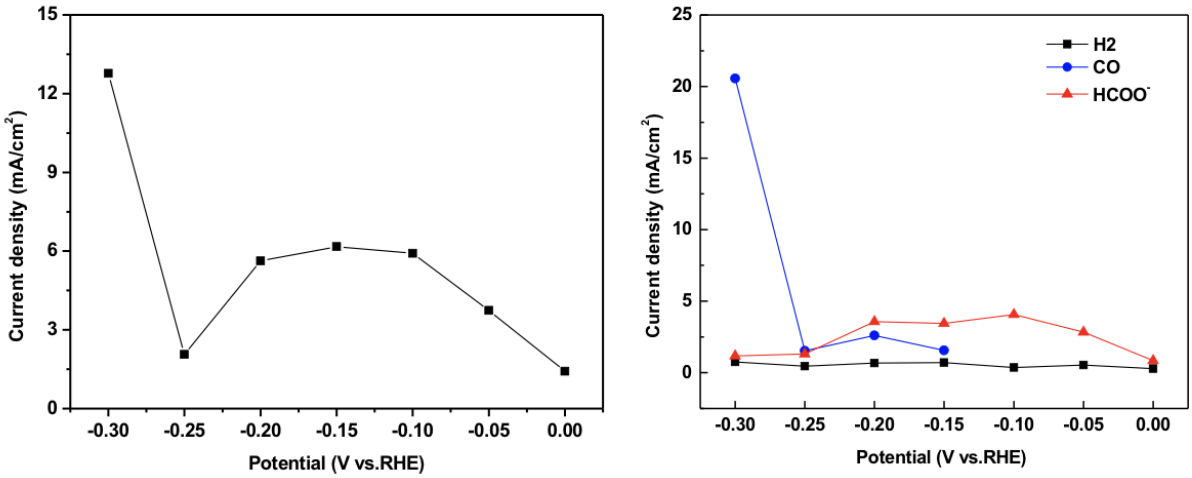

Figure 3.10 Geometric current density at the 300th second (left), partial current density for specific product (right) on Au@Pd NSs 2.

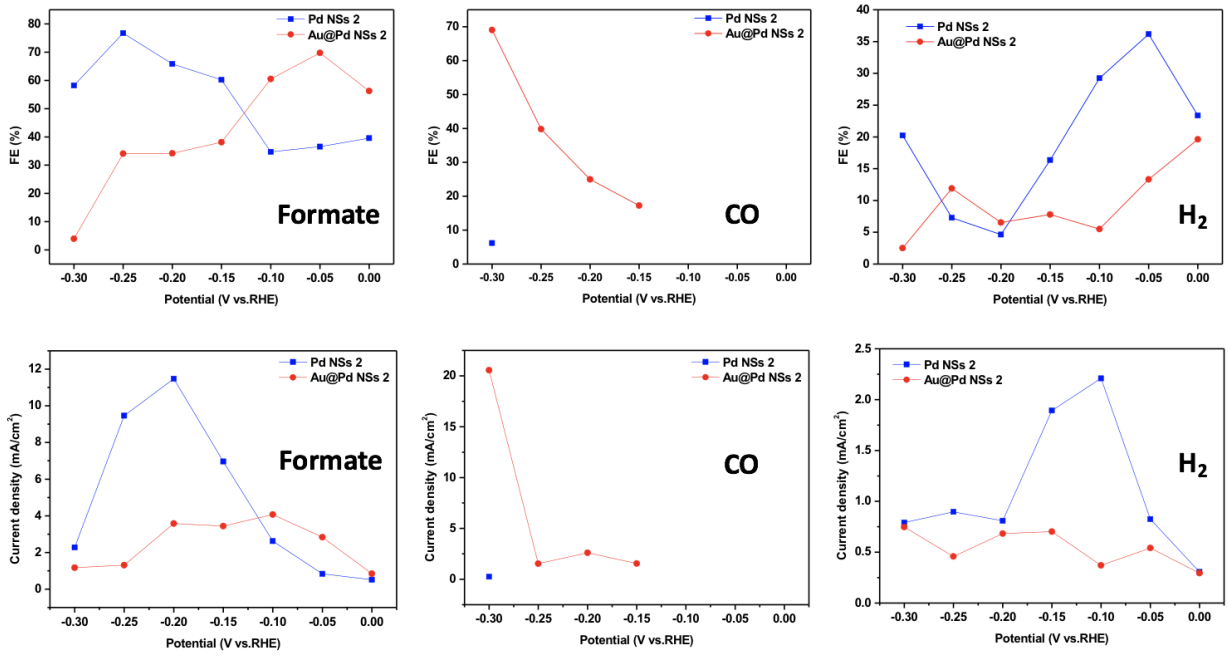

Figure 3.11 Comparison of Pd NSs 2 and Au@Pd NSs 2 in FE and partial current density.

By comparing the faradaic efficiency and partial current density towards different products between Pd NSs 2 and Au@ Pd NSs 2 (in Fig 3.11), the effects of growing Au on the catalytic performance regarding CO_2 reduction could be summarized as following: the hydrogen evolution reaction is suppressed on all applied potential. The selectivity towards formate increases in the low overpotential range, and CO is gradually become the dominate reduction product at high overpotential range.

4. Conclusions

Pd nanosheets (Pd NSs) with different thickness and in-plane compressive strain, as well as gold growing on the Pd nanosheets (Au@Pd NSs) have been successfully synthesized through the organic solvothermal method. These Pd-based nanosheets were characterized by Transmission Electron Microscopy (TEM), High Resolution Transmission Electron Microscopy (HRTEM), Inductively Coupled Plasma Mass Spectrometry (ICP-MS) and Energy Dispersive X-ray Spectrometry (EDS). Catalytic performance of Pd NSs and Au@Pd NSs towards formic acid oxidation and CO_2 reduction have been studied: Pd NSs could serve as efficient electrocatalysts towards formic acid oxidation with higher mass activity, stability and CO tolerance than the Pd commercial. Though their performance for CO_2 reduction has not meet the general requirement yet, they still have the potential to be applied for CO_2RR. More systematic research is needed to study the strain and synergistic effects on the CO_2RR.

5. Reference

1. Makhlouf, Abdel Salam Hamdy, and Ahmed Barhoum, eds. *Fundamentals of nanoparticles: classifications, synthesis methods, properties and characterization*. William Andrew, 2018.
2. Aliofkhazraei, M., and N. Ali. "Fabrication of micro/nanostructured coatings by CVD techniques." (2014): 85-117, doi: 10.1016/B978-0-08-096532-1.00706-8.
3. Reid, Jon, et al. "Factors influencing damascene feature fill using copper PVD and electroplating." Solid State Technology 43.7 (2000): 86-86.
4. Myerson, Allan. Handbook of industrial crystallization. Butterworth-Heinemann, 2002.
5. Harada, Masafumi, and Etsuko Katagiri. "Mechanism of silver particle formation during photoreduction using in situ time-resolved SAXS analysis." Langmuir 26.23 (2010): 17896-17905, doi: 10.1021/la102705h.
6. Tan, Chaoliang, et al. "Recent advances in ultrathin two-dimensional nanomaterials." *Chemical reviews* 117.9 (2017): 6225-6331, doi: 10.1021/acs.chemrev.6b00558.
7. Chia, Xinyi, and Martin Pumera. "Characteristics and performance of two-dimensional materials for electrocatalysis." *Nature Catalysis* 1.12 (2018): 909-921, doi: 10.1038/s41929-018-0181-7.
8. Jin, Huanyu, et al. "Emerging two-dimensional nanomaterials for electrocatalysis." *Chemical reviews* 118.13 (2018): 6337-6408, doi: 10.1021/acs.chemrev.7b00689.
9. Wang, Lei, et al. "Tunable intrinsic strain in two-dimensional transition metal electrocatalysts." Science 363.6429 (2019): 870-874, doi: 10.1126/science.aat8051.

10. " Fuel cells: why study fuel cells. " Energy Gov, 2020. https://www.energy.gov/eere/fuelcells/fuel-cells.
11. "Hydrogen storage: how hydrogen storage works. " Energy Gov, 2020. https://www.energy.gov/eere/fuelcells/hydrogen-storage.
12. Zhao, Xuxin, et al. "High-temperature passive direct methanol fuel cells operating with concentrated fuels." Journal of Power Sources 273 (2015): 517-521, doi:10.1016/j.jpowsour.2014.09.128.
13. Elnabawy, Ahmed O., et al. "Structure Sensitivity of Formic Acid Electrooxidation on Transition Metal Surfaces: A First-Principles Study." Journal of the Electrochemical Society 165.15 (2018), doi: 10.1149/2.0161815jes.
14. Elnabawy, Ahmed O., et al. "Structure Sensitivity of Formic Acid Electrooxidation on Transition Metal Surfaces: A First-Principles Study." Journal of the Electrochemical Society 165.15 (2018), doi: 10.1149/2.0161815jes.
15. Yu, Xingwen, and Peter G. Pickup. "Recent advances in direct formic acid fuel cells (DFAFC)." Journal of Power Sources 182.1 (2008): 124-132, doi: 10.1016/j.jpowsour.2008.03.075.
16. Kang, Yijin, et al. "Highly active Pt3Pb and core–shell Pt3Pb–Pt electrocatalysts for formic acid oxidation." ACS nano 6.3 (2012): 2818-2825, doi: 10.1021/nn3003373.
17. " Sea level. " NASA global climate change, 2020. https://climate.nasa.gov/vital-signs/sea-level/.
18. Gao, Dunfeng, et al. "Size-dependent electrocatalytic reduction of CO2 over Pd nanoparticles." *Journal of the American Chemical Society* 137.13 (2015): 4288-4291, doi: 10.1021/jacs.5b00046.

19. De Luna, Phil, et al. "What would it take for renewably powered electrosynthesis to displace petrochemical processes?" Science 364.6438 (2019): eaav3506, doi: 10.1126/science.aav3506.
20. Kuhl, Kendra P., et al. "New insights into the electrochemical reduction of carbon dioxide on metallic copper surfaces." Energy & Environmental Science 5.5 (2012): 7050-7059, doi: 10.1039/C2EE21234J.
21. Gattrell, M., N. Gupta, and A. Co. "A review of the aqueous electrochemical reduction of CO2 to hydrocarbons at copper." *Journal of Electroanalytical Chemistry* 594.1 (2006): 1-19, doi: 10.1016/j.jelechem.2006.05.013.
22. Gao, Dunfeng, et al. "Pd-containing nanostructures for electrochemical CO2 reduction reaction." *ACS Catalysis* 8.2 (2018): 1510-1519, doi: 10.1021/acscatal.7b03612.
23. Min, Xiaoquan, and Matthew W. Kanan. "Pd-catalyzed electrohydrogenation of carbon dioxide to formate: high mass activity at low overpotential and identification of the deactivation pathway." *Journal of the American Chemical Society* 137.14 (2015): 4701-4708, doi: 10.1021/ja511890h.
24. Kortlever, Ruud, et al. "Electrochemical CO2 reduction to formic acid at low overpotential and with high faradaic efficiency on carbon-supported bimetallic Pd–Pt nanoparticles." *Acs Catalysis* 5.7 (2015): 3916-3923, doi: 10.1021/acscatal.5b00602.
25. Wang, Yuxuan, et al. "Ensemble Effect in Bimetallic Electrocatalysts for CO2 Reduction." *Journal of the American Chemical Society* 141.42 (2019): 16635-16642, doi: 10.1021/jacs.9b05766.

26. Ge, Xiaoming, et al. "Oxygen reduction in alkaline media: from mechanisms to recent advances of catalysts." Acs Catalysis 5.8 (2015): 4643-4667, doi: 10.1021/acscatal.5b00524.
27. Qiu, Xiaoyu, et al. "One-Pot Synthesis of Freestanding Porous Palladium Nanosheets as Highly Efficient Electrocatalysts for Formic Acid Oxidation." *Advanced Functional Materials* 27.1 (2017): 1603852, doi: 10.1002/adfm.201603852.
28. Xu, Dan, et al. "Composition-dependent electrocatalytic activity of Pt-Cu nanocube catalysts for formic acid oxidation." Angewandte Chemie International Edition 49.7 (2010): 1282-1285, doi: 10.1002/anie.200905248.

Curriculum Vita

Wenqi Zhou

Department of Chemical & Biomolecular Engineering

The Johns Hopkins University, 3400 N. Charles Street, Baltimore, MD 21218, USA

Tel: (410) 8003712 • E-mail: wzhou23@ jhu.edu

Education:

Aug 2018 - May 2020 Master of Engineering, Johns Hopkins University, United states

Major: Chemical & Biomolecular Engineering

Sep 2014 - Jul 2018 Bachelor, Northwest Univeristy , China

Major: Food Science and Engineering